FY22 EIC Generic Detector R&D-09
Development of Thin-Gap MPGDs for EIC Trackers
Final Report

K. Gnanvo*[1], X. Bai[2], M. Dao[2], S.J. Lee[1], N. Liyanage[2], J. Nam[3], H. Nguyen[2], M. Posik[3], N. Smirnov[5], and S. Tarafdar[4]

[1]Thomas Jefferson National Accelerator Facility, Newport News, VA 23606, USA
[2]University of Virginia, Department Of Physics, Charlottesville VA 22903, USA
[3]Temple University, Philadelphia, PA 23606, USA
[4]Vanderbilt University, Department of Physics and Astronomy, Nashville, TN 37240, USA
[5]Yale University, Physics Department, New Haven, CT 06520, USA

December 21, 2023

Abstract

The EIC physics program requires precision tracking and PID over a large kinematic acceptance, as highlighted in the Yellow Report [1]. MPGDs are able to provide space point measurements to aid in both tracking and PID. These MPGD detectors will span a large pseudorapidity range (e.g. angular acceptance) and will see tracks entering over a large angular range, in addition to tracks bending due to the EIC's magnetic field. The position measured by an MPGD structure for a track impinging at a large angle is no longer determined by the detector structure (e.g. readout structure) but the gap in the ionization gas volume that the particle traverses before reaching the amplification stage, leading to a deterioration in the spatial resolution that grows with the angle. To minimize the impact of the track angle on the resolution, several thin-gap MPGDs (tg-MPGDs)prototypes, where the ionization gas volume is significantly reduced with respect to typical MPGD detectors, will be built and tested under beam condition. In addition various gas mixtures will be studied within simulation to identify optimal mixtures for future use.

The thin-gap MPGD (tg-MPGD) Consortium

Project Name: Development of thin-gap MPGDs for an EIC tracking detector

Project Period: from 10/1/2022 to 09/30/2023

PI & Contact Person: Kondo Gnanvo; kagnanvo@jlab.org

*kagnanvo@jlab.org

Contents

1 What was planned

Our R&D goal for the FY22 proposal is to demonstrate the proof of concept of thin Gap MPGDs (tg-MPGDs) by developing and testing in beam several prototypes based on all three MPGD amplification structures with different gas mixtures. The test in beam include study of the spatial resolution performance as a function of the incoming angle of the beam as well as HV scan for gain optimization of the prototypes. The tasks and responsibilities of each institutions is listed below

2 What was achieved - Development of thin-gap MPGDs

2.1 Development of tg-µRWELL prototypes at JLab

2.1.1 tg-µRWELL prototypes and capacitive-sharing readout

JLab assembled three µRWELL-based thin-gap prototypes, one with single-amplification µRWELL amplification structure and two prototypes with hybrid amplification structures combining a pre-amplification GEM on top of main amplification µRWELL PCB layer. The configuration of the prototypes are tabulated in table 1 The cross sectional schematic view for both the single-amplification thin-gap µRWELL and

JLab thin gap prototypes			
Prototypes	Drift gap [mm]	Induction gap [mm]	Funding source
Proto I: GEM-µRWELL hybrid	1.0	1.0	EIC generic R&D
Proto II: GEM-µRWELL hybrid	0.5	1.0	EIC generic R&D
Proto III: µRWELL - single	1.0	N/A	EIC generic R&D
Ref Det: std-µRWELL	3.0	N/A	RD&I Group

Table 1: JLab thin-gap prototypes along with funding source

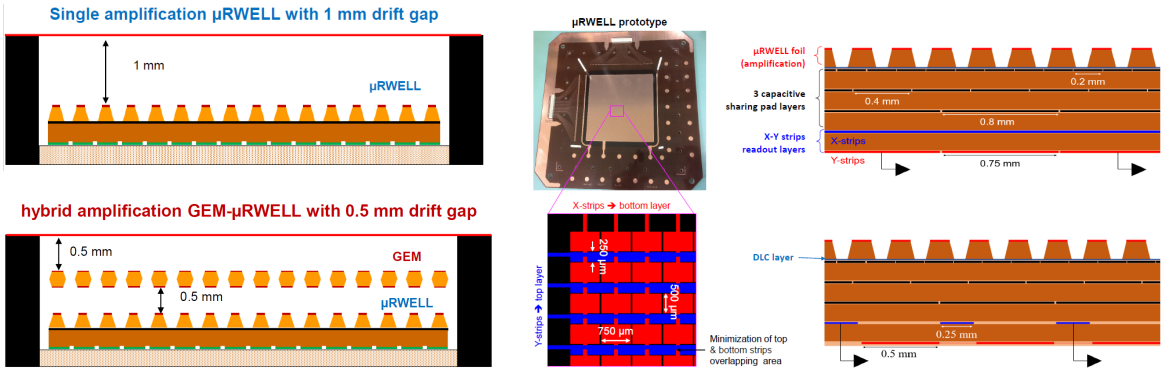

Figure 1: (*left*) Cross sectional view of 1-mm thin-gap µRWELL (top) and of a 1-mm thin-gap GEM-µRWELL hybrid; (*center*) µRWELL PCB (top) with capacitive-sharing X-Y readout structures (bottom); (*Right*) cross-sectional view of capacitive-sharing readout, x-strips view (top) and y-strip view (bottom)

double-amplification thin-gap GEM-µRWELL hybrid is illustrated in the left of Fig. 1. All prototypes listed in table 1 are based on the same µRWELL PCB shown in the picture (top center) with the Gerber views

of the capacitive-sharing X-Y strip readout (bottom center). Cross sectional views of the capacitive-sharing X-Y strip readout [2], which allows reduction of number of readout channels) without degradation of the spatial resolution performance of the detector are shown on the right of Fig. 1. A few steps for the assembly

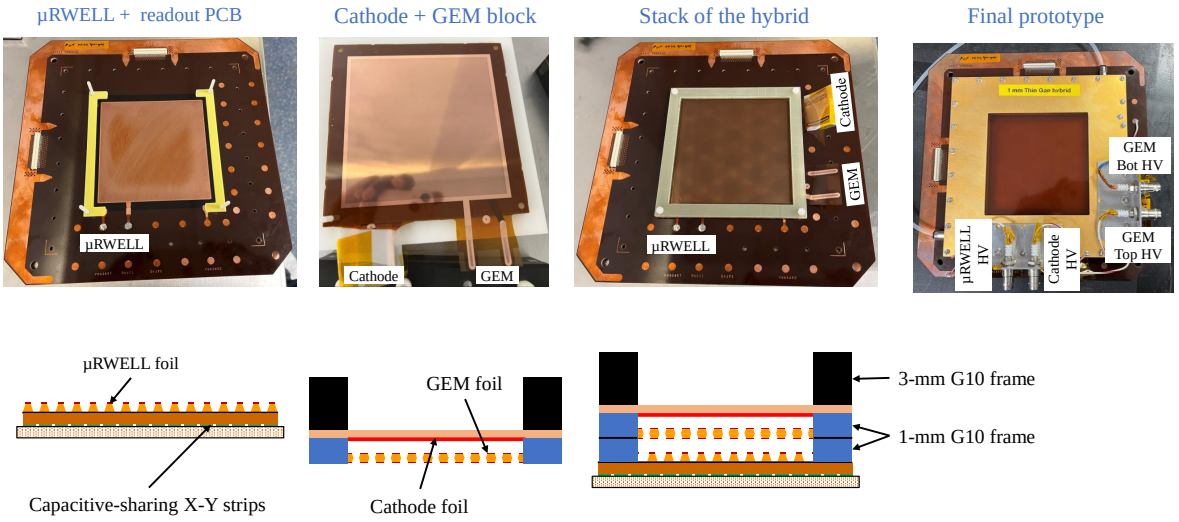

Figure 2: Assembly in clean room of 1-mm thin-gap GEM-μRWELL hybrid prototype: (*left*) μRWELL PCB with capacitive-sharing X-Y strip readout; (*center Left*) block of drift cathode and pre-amplifier GEM foils glued to a thick G10 frame; (*center right*) stack of the μRWELL PCB and the cathode-GEM block; (*right*) Prototype in gas box with 4 SHV connectors for HV supply of the cathode, GEM and μRWELL.

in clean room of the prototypes are briefly described in Fig. 2. The μRWELL PCB, GEM foil and gas box are procured from CERN MPGD workshop, the support frames were fabricated at JLab machine shop and the final assembly was done in the JLab RD&I clean room laboratory. Basic HV tests were performed on the prototypes in JLab RD&I MPGD detector lab before the prototypes were transported to the test beam at Fermilab for comprehensive characterization.

2.1.2 Tracker telescope setup with Y-axis rotation stage

Jlab developed a rotation stage that can rotate up to three MPGDs at the same time. The stage was made using aluminum extrusion rails (also known as 80/20). Depending on the supporting weight, either 20 mm x 20 mm or 40 mm x 20 mm profile was used. The size of main frame is 70 cm x 60 cm x 70 cm and the distance between each MPGD mounting frame is 20 cm. Three MPGD mounting frames were connected by a linkage that makes the same rotation angle for all three mounting frames. The rotation stage has worm/spur gears of 180:1 gear ratio and is run by a stepper motor with a 1.8 degree step angle. The stepper motor was controlled with a GRBL open source motion controller. The resolution of rotation stage is 0.01 degree/step and the estimated backlash is 0.1 degree. The controller was connected to a PC by a USB port and run by an open source software. For the experiment at FTBF, an Ethernet based USB extender was used to control the stage from the control room. A USB webcam was attached to the rotation stage to monitor the rotation stage from the control room. An overview of rotation stage is shown in Fig. 3.

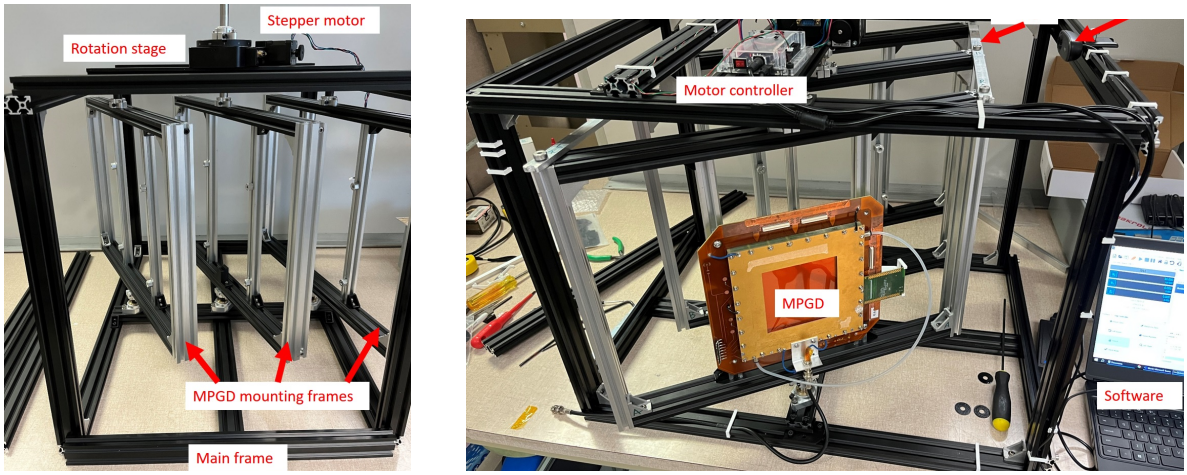

Figure 3: *Left* Picture of rotation stage with three MPGD mounting frames. *Right* Picture of added MPGD on the front frame, a stepper motor controller, and a webcam

2.2 Development of tg-μRWELL prototypes at Vanderbilt U.

2.2.1 Prototypes

Vanderbilt assembled three prototypes based on 2D zigzag strips using μRWELL, Micromegas and GEM. The configuration of the prototypes are tabulated in table 2

Vanderbilt thin gap prototypes			
Prototypes	Drift gap [mm]	Transfer gap [mm]	Funding source
Proto I: GEM-μRWELL hybrid	1.0	0.5	EIC generic R&D
Proto II: μRWELL	1.0	N/A	EIC generic R&D
Proto III: GEM-MMG hybrid	1.0	1.0	Vanderbilt

Table 2: Types of Vanderbilt thin gap prototypes along with funding source

All the three prototypes by Vanderbilt were based on 2D zigzag readout out with 1.6 mm pitch which allowed for lesser number of channels. Fig. 4 shows the μRWELL layer along with Gerber diagram of 2D zigzag readout. The 2D zigzag readout board resembles X-Y strip pattern as shown in the right side of the figure 4.

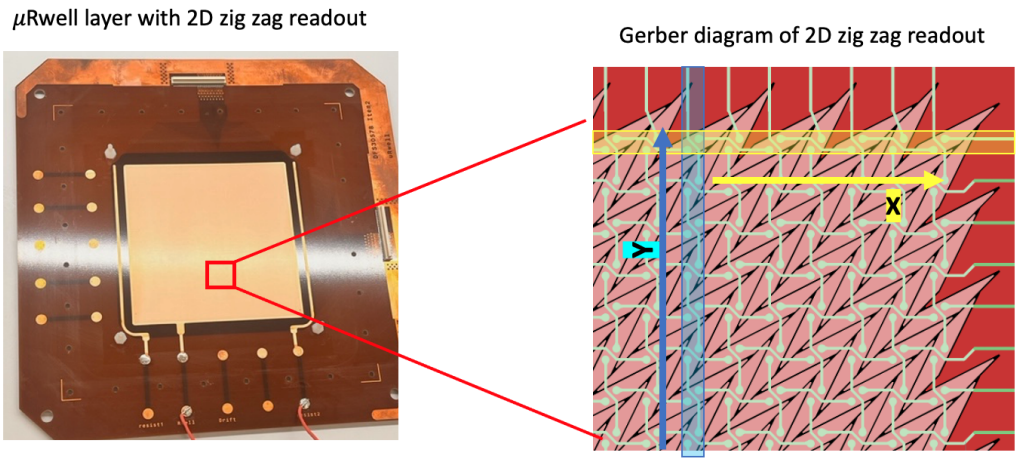

Figure 4: *Left* Picture of 2D zigzag readout PCB with μRWELL layer. *Right* Gerber diagram of 2D zigzag readout with X-Y pattern with 1.6 mm (not to scale) pitch.

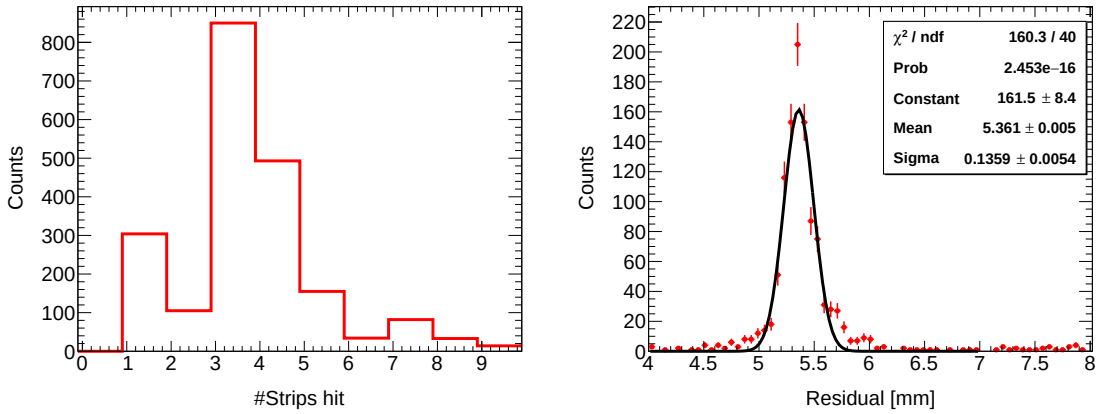

Figure 5: *Left* Number of strips fired on X-ray test bench with 1.5 keV X-ray photons radiating 3 mm drift gap 2D zig zag readout μRWELL detector. *Right* Resulting residual distribution with width of 136 um

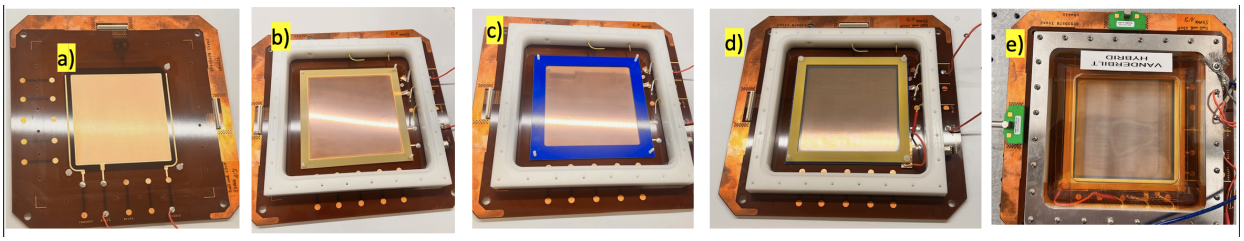

Figure 6: *a)* Standalone μRWELL layer with 2d zigzag readout. *b)* GEM foil and gas box mounted on μRWELL layer.*c)* Spacer (in blue color) between GEM foil and drift cathode mounted on GEM foil. *d)* Drift cathode mesh mounted on GEM foil.*e)* Final gas sealed thin gap hynbrid prototype.

The 2D zigzag strip design was motivated from in-house test bench study using X-ray as primary ionizing source for 3 mm drift gap μRWELL detector in Ar-CO_2 (80:20) gas mixture. The energy of X-ray was

reduced to 1.5 keV . Left plot in Fig. 5 shows the number of strips fired in the test set up while the right hand plot shows the residual distribution with sigma of 135 microns after selecting number of strips between between 3 and 6. µRWELL with 2D zigzag readout boards, drift cathode made of stainless steel mesh and 10 cm x 10 cm active area GEM foil were procured from CERN. The gas box and spacers were machined in Vanderbilt machine shop. Fig. 6 shows the pictorial representation of various steps for assembling the GEM-µRWELL hybrid prototype

The cost associated with the items for assembling the prototypes are tabulated in table 3

Expenses for Vanderbilt thin gap prototypes only	
Items	Expenses
2 x µRWELL	9500.00 USD
3 x drift mesh	745.00 USD
Machine shop and items	1920.00 USD

Table 3: Approximate expenses for assembling prototypes

2.3 Development of Thin-gap Triple-GEM prototypes at UVa

2.3.1 Introduction of plans

A highly effective way to maintain thin gaps between cathodes and anodes in large-area detectors is the use of cathodes made of fine wires or fine wire mesh. In order to investigate the performance of triple-GEM detectors at large acceptance with different drift gaps as well as to explore different cathode structures to maintain the small gap between the cathode layer and the amplification region, UVA has constructed four 10 cm $\times$ 10 cm Thin-Gap triple-GEM prototypes. The first two prototypes utilize cathode layers made of standard Copper-Kapton foil and have a drift gap between the cathode and the uppermost GEM foil measuring 1.5 mm and 1.0 mm. The third and fourth prototypes employ cathodes made of fine wires with wire pitches of 400 μm and 800 μm, maintaining a drift gap of 1.5 mm. Fig. 7 displays images of these triple-GEM prototypes with different cathode configurations. Details about the configuration of UVA prototypes are listed in Table 4

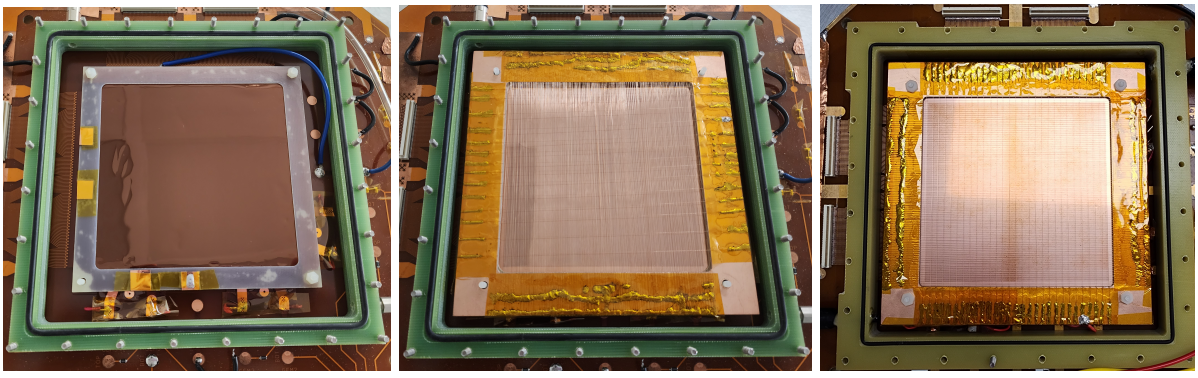

Figure 7: Prototypes with standard Copper-Kapton foil (*left*), 400 μm wire-pitch cathode (*center*), and 800 μm wire-pitch cathode (*right*).

UVA Prototypes		
Prototypes	Drift gap (mm)	Cathode
Proto I: Thin-gap Triple-GEMs	1.0	Kapton foil with 5 μm copper coating
Proto II: Thin-gap Triple-GEMs	1.5	Kapton foil with 5 μm copper coating
Proto III: Thin-gap Triple-GEMs	1.5	400 μm-pitch wire
Proto IV: Thin-gap Triple-GEMs	1.5	800 μm-pitch wire
Ref Det: Standard Triple-GEMs	3.0	Kapton foil with 5 μm copper coating

Table 4: UVA Thin-gap Triple-GEM Prototypes

2.3.2 Structure and operation of UVA prototypes

Each of Triple-GEM prototype assembled at UVA consists of three layers of GEM foils separated by 2 mm, a readout board 2 mm below the bottom GEM foil, and a drift cathode layer above the top GEM foil. The microscope photographs in Fig. 8(a) and Fig. 8(b) show the hole structure of GEM foils and the two-dimensional strip pattern of the readout boards used in our prototypes. All GEM and cathode electrodes of a prototype are powered from a single high-voltage source through a resistive voltage divider as shown in Fig. 8(c). The resistances of the divider were designed such that during the operation, the electric field in the GEM foils increased by a step of 22% from the bottom GEM foil towards the top GEM foil, and the electric field in the transfer and induction regions was 33% higher than in drift region.

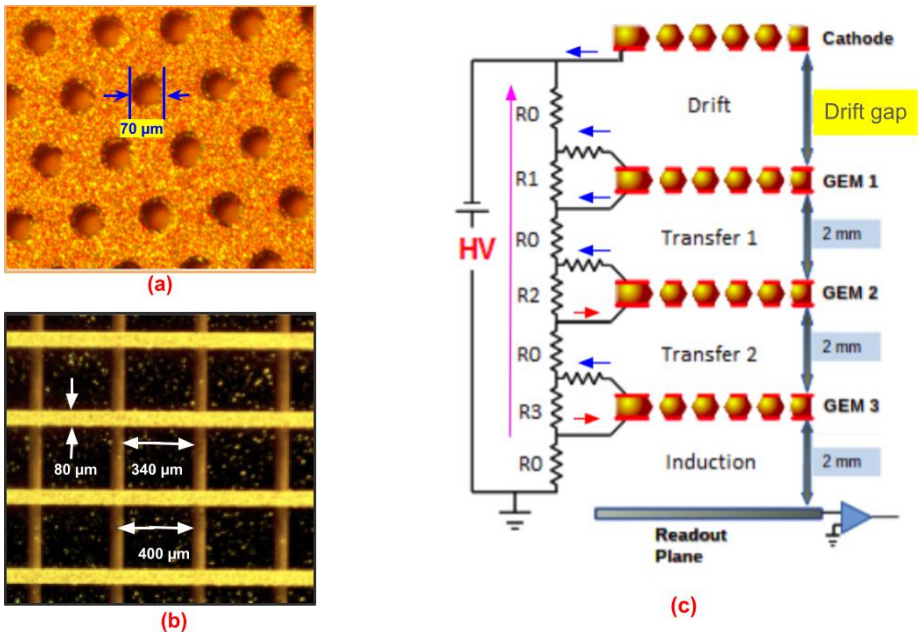

Figure 8: Structure of GEM holes(a), two-dimensional pattern of the readout boards(b), and resistive voltage divider(c).

The preliminary examinations on the efficiency and the high voltage stability of four prototypes, as well as the optimization of DAQ system for taking data at a high rate and doing online data analysis, were conducted in the Detector lab at UVA using cosmic and X-ray sources.

3 What was achieved: Fermilab Test beam - June 2023

3.1 Test beam setups

Eight of the ten thin-gap MPGD prototype, described in 2.1.1, 2.2, 2.3 were installed in the MT6.2b area of the Fermilab test Beam Facility (FTBF) and were tested using the 120 GeV primary proton beam from June 14 - 20 2023. Two tracking telescopes setups were assembled to simultaneously test up to five prototypes during the campaign. Each telescope consisted of the prototypes under study, sandwiched between two pairs of standard 10 cm $\times$ 10 cm CERN GEM trackers [3], one pair upstream and one pair downstream. Setup **I** as shown picture on the left on Fig. 9 was dedicated to the studies of basic characteristics of the prototypes such as gain curve, strip multiplicity and X-Y charge-sharing as a function of HV scan applied to the amplification structures. On this setup, two prototypes were tested at the time. Setup II of on the right of Fig. 9 was dedicated to the study of spatial resolution of the prototypes as a function of the angle of incoming particle with respect to the normal axis of the prototypes. On this setup II, three prototypes were installed on the rotation stand (as described in section 2.1.2), sandwiched between one pair of upstream GEM trackers and one pair of downstream GEM trackers. The rotation stand allow the rotation along the vertical axis of the plane of the prototypes under study by step of 1 to 6 degrees up to $\pm$45 degree with respect to the proton beam axis for the study of the impact of track angle on the spatial resolution performance of the thin-gap prototypes. All detectors on the two set ups were operated with $ArCO_2$ (80:20) gas mixture. Only the thin gap prototypes by UVA and VU were also operated partially with $KrCO_2$ (80:20) gas mixture to study the effect of heavier gas on detector efficiency. Each setup was equipped with one APV25-based [4]

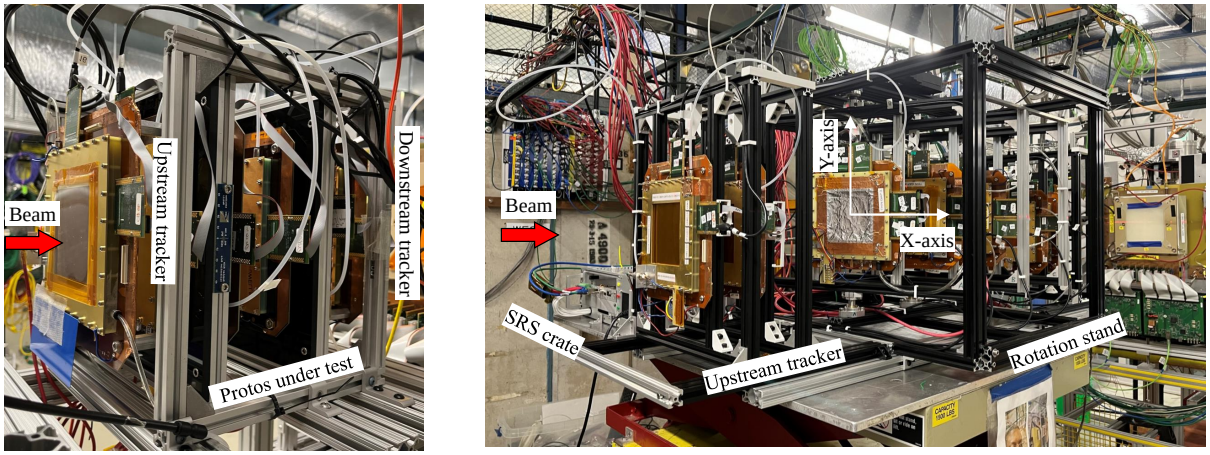

Setup I: HV scan runs

Setup II: Angle scan runs

Figure 9: Thin-gap MPGD tested in beam at the FTBF, consisting on two separate tracking telescope setups: Setup I: HV scan for gain and performance characteristics studies of the prototypes on setup I (*left*); setup II: with rotation stand for track angle scan of the prototypes (*right*).

Scalable Readout System (SRS) [5] crate, the readout electronics developed by CERN RD51 collaboration [6] for MPGDs. Each crate has 16 APV25 front end cards and read out up to 2048 channels. Two different data acquisition system were used during the beam test campaign. The DAQ and monitoring software packages, DATE and amoreSRS, both legacy software developed by the ALICE collaboration at CERN [7], were used for JLab thin-gap prototypes runs. For UVa and VU prototype runs, a CODA-based GEM DAQ and decoder were used; both of them are legacy of the JLab Hall B PRad [8] experiment GEM DAQ system [9]. The CODA-based GEM DAQ features a higher trigger rate with a bottleneck mainly coming from the data bandwidth between the SRS crate and the DAQ computer. In the Fermilab test, a roughly 1 kHz trigger rate for 9 time sample data, and 1.5 kHz for 6 time sample data were observed, both with a total of 16 APVs. The trigger for the SRS crates was provided by the coincidence signal formed by a set of three

trigger counters of installed at the MT6.2b area. The sampling rate of the APV25 signal was 50 ns for the data acquisition and nine APV25 time samples were recorded per readout channel which correspond to an acquisition window of 450 ns. Both amoreSRS and GEMViewer software packages include scripts for decoding raw APV25 raw data, applying common mode correction, pedestal offset subtraction and zero suppression and processing the data to produce performance characteristic plots for MPGDs. Both software packages are capable of online monitoring, providing the ability to check the quality of live events, reset runs when APV cards malfunction, and maximize the usage of beam time.

3.2 Gas mixing system

The gas supply to Setup II as shown in right side of Fig. 9 was done through gas mixing unit capable of mixing two different gas at various proportion. The schematics of the gas mixing unit is shown in fig. 10 and was designed and assembled in house by Vanderbilt and Yale University. The mixing ratio is determined by the flow rate controlled by Mass Flow Controllers labelled as **MFC1** and **MFC2** in fig. 10. The output pressure from the gas bottles was maintained at below 10 psi. To avoid accidental increase in pressure inside the gas mixing unit components the inlets to the Mass Flow Controllers were fitted with safety relief pressure valves labelled as **PR12**. In order to have minimum pressure inside the detectors the inlet to detector line from gas mixing unit has pressure relief bubbler. Further to monitor both oxygen and water content in the gas itself the gas mixing unit had both O_2 and H_2O monitors.

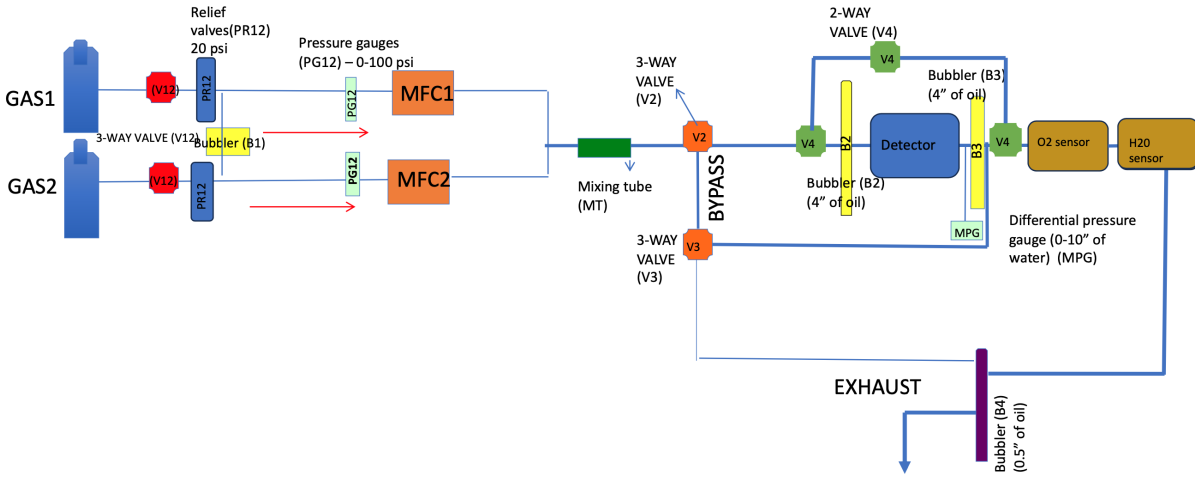

Figure 10: Schematics of gas mixing unit used in Fermilab Test beam campaign for testing thin gap prototypes.

3.3 Test beam runs

The different runs at the Fermilab test beam associated to different prototypes are listed on the table 5. For most data runs, the prototypes operated with Ar-CO_2 (80:20) gas mixture, except for one 8-hour shift runs were Kr-CO_2 (80:20) gas mixture. Single amplification thin-gap μRWELL prototypes from JLab and Vanderbilt were not tested in beam because of the short period of beam time that was made available to us. The priority went to the double-amplification GEM-μRWELL and GEM-Micromegas hybrid prototypes that we determine were the most likely to results in the best performances in term of spatial resolution and detector efficiency.

Prototypes	Ar-CO_2	Kr-CO_2	HV scan	Angle scan
JLab Proto I	YES	NO	μRWELL HV, GEM HV, drift field, induction field	0 to 45°
JLab Proto II	YES	NO	μRWELL HV, GEM HV, drift field, induction field	0 to 45°
JLab Ref Det	YES	NO	NO	0 to 45°
VU Proto I	YES	YES	μRWELL HV, GEM HV	0 to 45°
VU Proto III	YES	YES	μMEGAS HV, GEM HV	0 to 45°
UVA Proto I	YES	NO	GEM HV	0 to 45°
UVA Proto II	YES	YES	GEM HV	0 to 45°
UVA Proto III	YES	NO	GEM HV	0 to 45°
UVA Proto IV	YES	NO	GEM HV	0 to 45°
UVA Ref Det	YES	NO	NO	0 to 45°

Table 5: Different types of runs for different types of thin-gap MPGDs at FTBF.

3.4 Results with JLab prototypes

The two JLab GEM-μRWELL hybrid prototypes were operated with Ar-CO_2 (80:20) gas mixture for all HV and angle scan runs. In order to compare the impact of thin-gap on position resolution, a standard gap 3-mm μRWELL detector was used as reference during the track angle scan run on setup II. The reference detector has the same readout strip pattern as the two prototypes. Performance characteristics of the detectors such as the ADC distribution, strip multiplicity and efficiency are produced after common mode correction, pedestal subtraction and zero suppression were applied to the raw APV25. At the beginning of each run, a pedestal run is performed to generate the pedestal data (pedestal offset and rms noise) for each individual APV25 channels. The pedestal data are store in a root file that is uploaded during the analysis for the common mode, pedestal subtraction and zero suppression algorithm.
For all plots discussed in this section, *(solid dots)* and *(open dots)* represent results on x-strip and y-strip planes respectively.

3.4.1 Efficiencies and strip multiplicity studies vs. high voltage scan

For the HV scan, we study the characteristic performance of the prototypes such as the mean value of the ADC charge distribution, the average strip multiplicity and detector efficiency. The different type of HV scan runs performed on the prototypes are as follows:

- **μRWELL HV scan:** voltage scan across the μRWELL electrode and the ground.
- **GEM HV scan:** voltage scan across the top and bottom electrode of the GEM foil.
- **Drift field scan:** voltage scan between the drift cathode and the GEM top electrode.
- **Induction field scan:** voltage scan between the GEM bottom electrode and the μRWELL electrode.

For the HV scan run, after applying common mode correction and pedestal subtraction , a 5 σ σ cut based on the pedestal RMS of individual APV25 channel is applied for zero suppression. Then a simple centre of gravity (COG) algorithm is performed on a cluster of consecutive strips to extract the particle position in both x and y planes of the detector. Single strip cluster are also included in the analysis of HV scan studies. The data for the 1-mm thin-gap GEM-μRWELL hybrid proto I are shown in *red*, the data for 0.5-mm thin-gap GEM-μRWELL hybrid proto II are shown in *blue* on all plots.

µRWELL HV scan

A scan of the bias voltage applied to µRWELL for both prototypes was performed from 380V to 475V in steps of 5V or 10 V during this run. The voltage applied across the pre-amplification GEM foil was kept to 350V and the electric field in the drift and induction region at 2kV / cm. The plots on the left of Fig. 11 shows the average charge in ADC counts in x- and y-plane of the two prototypes as a function of the applied voltage. For both prototypes, the signal collected by the strips in x-plane is slightly higher than in y-plane. This non equal sharing of the charges in x and plane can be explained by geometrical consideration of the two-layer design of the X-Y strip readout which is identical for the two prototypes I and II. With the current design, the width of the top layer is too large and pick up more than half of the total induced charges from the amplification layers. The relative width of top and bottom strip layers can be easily optimized in the future for a more equal charge sharing. The charges collected by the readout planes of proto I (red curves) are significantly higher than for proto II (blue curves) for the same HV setting because of the larger primary ionization charges in the 1-mm drift gap of proto I than the 0.5-mm drift gap of proto II.

The strip multiplicity, which is defined as the average number of strips with hit above threshold in the

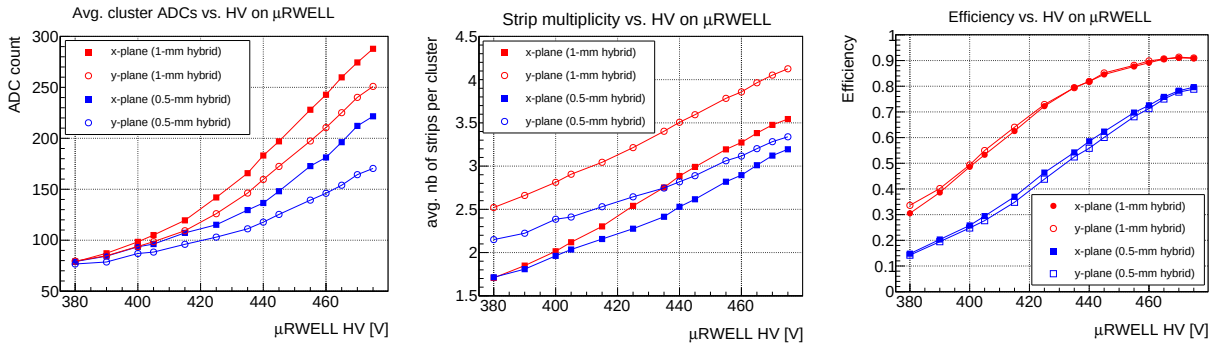

Figure 11: Characteristics plots of the thin-gap prototypes as a function of the bias voltage applied to the µRWELL amplification foil: Average cluster charges in ADC counts (*left*); average strip multiplicity per event (*center*); detector efficiency per readout plane (*right*).

cluster per event, is plotted as a function of the µRWELL voltage for the two prototypes in the graphs in the center of Fig. 11. In this analysis, single-strip cluster are included and this explains that for the lower voltage setting at 380V, the strip multiplicity is 1.5 for x-plane strips. For the y-planes, the strip multiplicity is 2.15 in 0.5-mm gap proto II and 2.5 in 1-mm gap proto I. The higher strip multiplicity in y-plane as compared to x-plane apparently contradicts the fact that charges collected by the strip in x-plane is higher than in y-plane. But this apparent contradiction can be easily explained by the distinctive feature of capacitive-sharing layer and the narrow size of the proton beam. All particles typically hit one pad of the top capacitive-sharing layer in the x direction and 2 pads in y direction and this feature is propagated all the way down to the strip layers. In all cases, the strip multiplicity increases linearly with the applied voltage on the µRWELL up to 4.2 and 3.6 in y-plane and x-plane respectively for proto I and 3.4 and 3.2 in y-plane and x-plane respectively for proto II when the µRWELL voltage reaches 475 V. Higher strip multiplicity can be easily obtained even for 0.5 mm thin-gap MPGDs with capacitive-sharing readout structures.

The efficiency curve in x-plane and y-plane for the two prototypes as a function of the µRWELL voltage is shown on the graphs at right of Fig. 11. The efficiency reaches its plateau at 90% in both x-plane and y-plane for the 1-mm gap prototype at HV = 460V. The plateau not reaching higher value than 90% even when increasing the HV value means that we reach the lower limit of one primary ionization cluster which is the real bottleneck for the maximum efficiency at 90% even when there is still enough margin to increase the gain capabilities of the two amplification prototypes. For the same reasons, the efficiency is significantly lower for the 0.5-mm gap prototype, where the plateau seems to be reached at around 80%. However in this case, we did not push the µRWELL voltage at higher value than 475 V to clearly see the full plateau region.

GEM HV scan

For this run, a scan of the voltage across the top and bottom electrode of the pre-amplification GEM foil for the two prototypes was performed from 300V to 370V by step of 10 V while the voltage on the µRWELL was kept at 460V and the electric field in the drift and induction region maintained at 2kV/cm. Like for the µRWELL voltage scan, the charge collected on the strips in x and y steadily increases with the HV on the GEM as shown on the left of Fig. 12, the curve follows an exponential shape. The signal amplitude in ADC

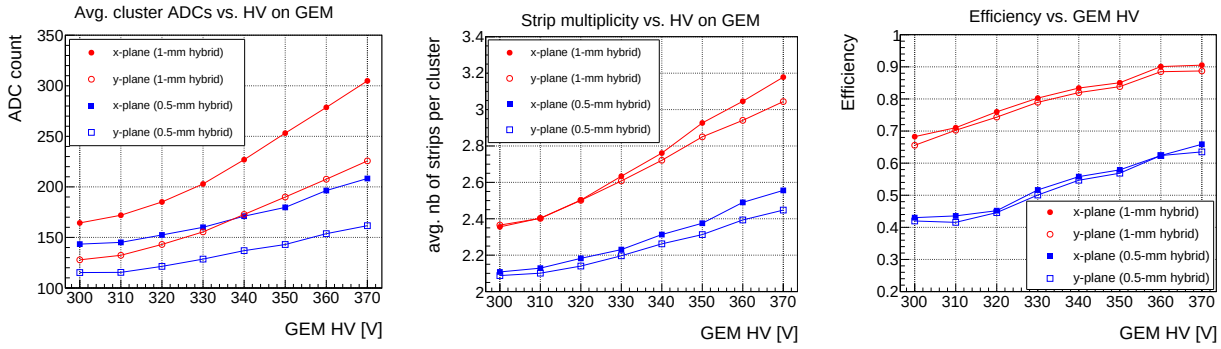

Figure 12: Characteristics plots of the thin-gap prototypes as a function of the bias voltage applied to the GEM pre-amplification foil: Average cluster charges in ADC counts (*left*); average strip multiplicity per event (*center*); detector efficiency per readout plane (*right*).

counts is about 33% smaller for the 0.5-mm gap prototype than the 1-mm gap at 370V. In the plots at the center of Fig. 12, the strip multiplicity also show linear increase with the GEM HV and reaches 3.2 and 3 on average in x-plane and y-plane respectively at 370V for proto I while significantly lower at 2.1 and 2.4 for proto II. Proto I reaches efficiency plateau at 90% for both x-plane and y-planes an HV = 370 V on the GEM foil,(right in Fig. 12), starting at lower than than 70% efficiency when 300 V is applied to the GEM. The efficiency at 370 V on the GEM is around 65% in both x- and y-plane for proto II far from reaching its plateau. We did not push the voltage on the GEM high enough to reach the efficiency plateau for this prototype.

Drift field scan:

A scan of the electric field in the drift region was also performed by varying the voltage applied to the cathode with respect to the voltage applied to the top electrode of the GEM foil. The field was increased

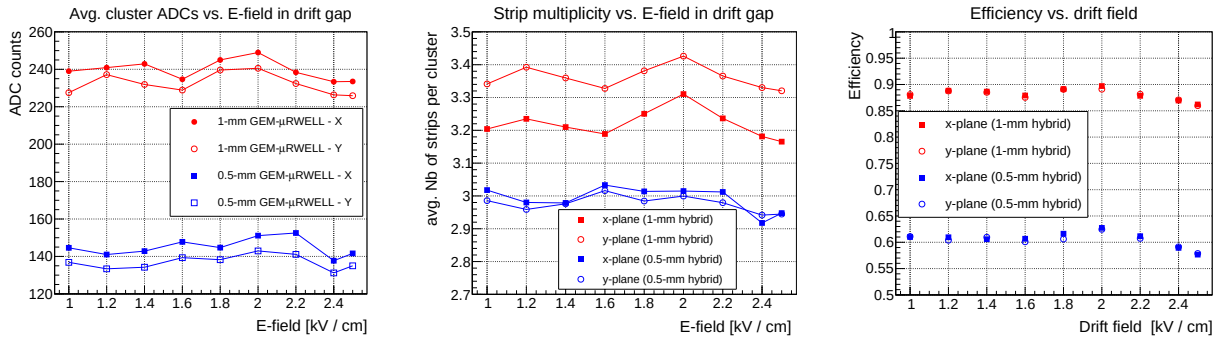

Figure 13: Characteristics plots of the thin-gap prototypes as a function of the electric field in the region between the cathode and the top electrode of the GEM foil: Average cluster charges in ADC counts (*left*); average strip multiplicity per event (*center*); detector efficiency per readout plane (*right*).

from 1 kV / cm in the drift region to 2.6 kV / cm in steps of 200 V. The voltage on the μRWELL and GEM foil were kept at 460 V and 350 V respectively and the electric field in the induction region was set to 1 kV / cm. As shown in the plots of Fig. 13, in this electric field range in the drift region, we did not observe a significant variation of the characteristic of the detectors. The efficiency reaches 90% for proto I at a field of 2 kV / cm but remain higher than 85% for all the other value for the electric field in the drift. The efficiency is lower for the 0.5-mm thin-gap prototype and also shows very little variation with the electric field.

Induction field scan

A scan of the electric field in the induction region has a more significant impact on the performance of the prototypes as shown in the plots of Fig. 14. For this run, we kept the voltage on the μRWELL and GEM foil at 460 V and 350 V respectively and the electric field in the drift region 2 kV / cm and vary the voltage applied to the bottom electrode of the GEM foil with respect to the bias voltage on μRWELL to scan the induction field from 1 kV to 2kV. Unlike the drift field scan, the signal amplitude (in ADC counts) increase

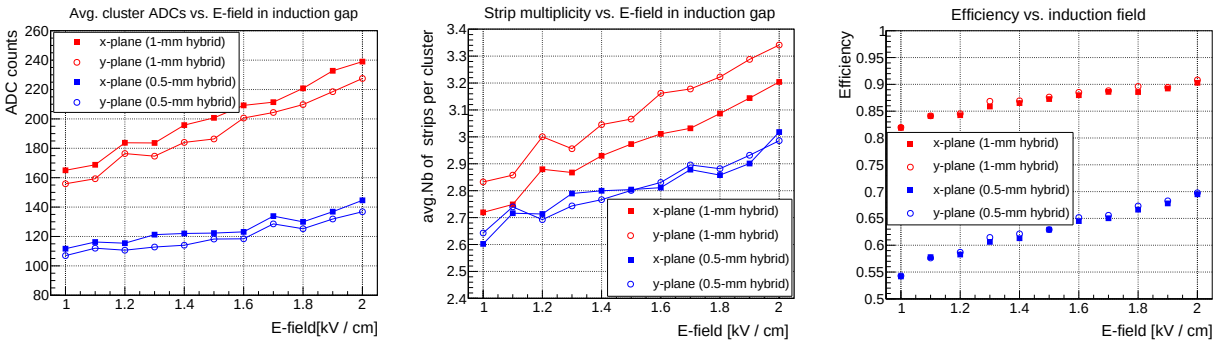

Figure 14: Characteristics plots of the thin-gap prototypes as a function of the electric field in the induction volume between the bottom of the GEM foil and the μRWELL PCB layer: average cluster charges in ADC counts (*left*); average strip multiplicity per event (*center*); detector efficiency per readout plane (*right*).

by 50%, from 160 to 240 ADC counts for proto I and from 90 to 140 ADC counts for proto II when the induction field increases from 1 kV / cm to 2 kV / cm as shown in the plots in the left of Fig. 14. The strip multiplicity in the middle plots of Fig. 14 also increases linearly by about 10 to 15% for both prototypes and the efficiency of proto I steadily increases from 80% to reach its plateau at 90% when the induction field increases from 1 kV / cm to 2 kV / cm.

3.4.2 Efficiency and strip multiplicity studies vs. angle scan

Fig. 15 shows the distribution plots of the strip multiplicity in x-plane (top in blue) and y(bottom plots in red) for the two thin-gap prototypes under test (left, middle)and the reference μRWELL detector (right) for the run when the proton beam was perpendicular to the planes of the prototypes track angle = 0^{circ}. The average strip multiplicity for the 1-mm thin-gap GEM-μRWELL prototype is 3.3 and 3.2 in x and in y respectively and is higher than for the 3-mm gap reference detector which is equal to 2.9 in both x and y. This is because 1-mm thin-gap GEM-μRWELL has double amplification and larger signal than the standard 3-mm μRWELL. In addition, the pre-amplification GEM foil also contributes to the lateral spread of the initial ionisation charge cluster which compensates the deficit caused by the narrower (1-mm) gap. For the same reason, we were able to measure an average strip multiplicity of 2.9 for the even thinner 0.5-mm thin-gap GEM-μRWELL prototype which is similar to the performance of the reference detector. For track angle = 0^{circ}, strip multiplicity in x and y are of the same order, however when the detector plane start rotating along y-axis with respect to track angle, the average strip multiplicity in both x-axis and y-axis of the three prototypes steadily increases as a function of the track angle as one would expect because the particles leaves a longer ionization trails as they traverses the detector gas volume. For that reason, the larger the drift gap

is, the longer the trail is and subsequently the larger the number of strips with hit associated to the event. On the plots on the left of 16, the average strip multiplicity as a function of the particle track angles which is normalised to the average strip multiplicity at the angle 0° in x and y plane for the three prototypes is shown. The increase of the average strip multiplicity in x-plane is significantly bigger for reference detector with 3-mm gap detector than for the thin gap prototypes as expected and also larger for the x-strip planes than y-strip planes. The detector efficiency also shows a strong dependence with the track angle as shown

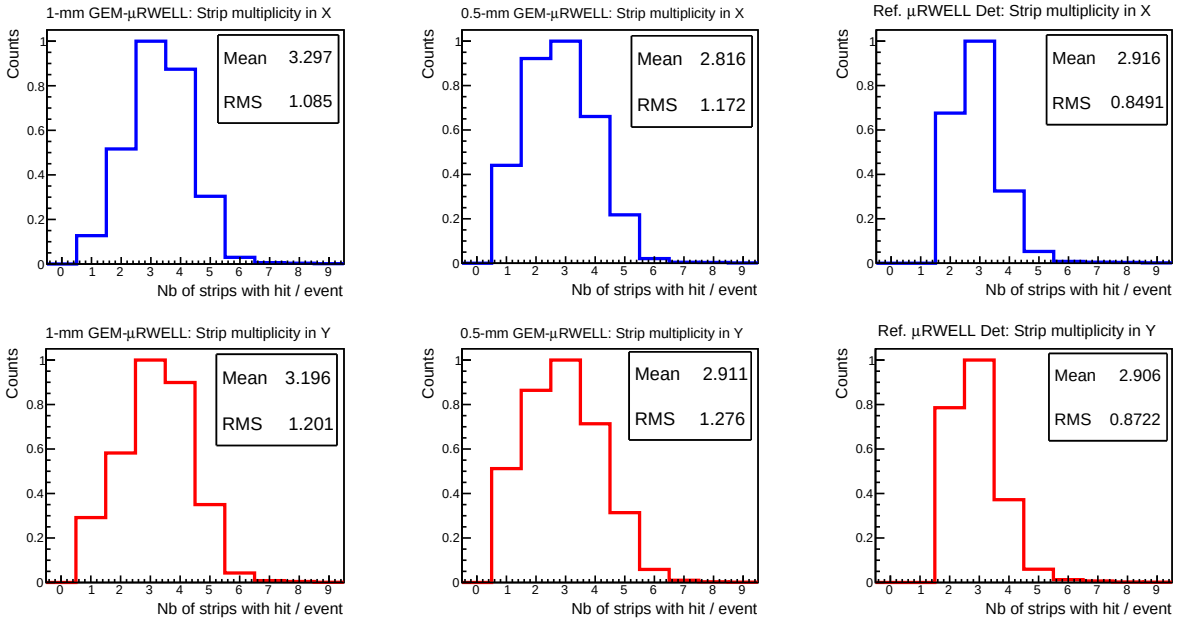

Figure 15: Strip multiplicity in x-plane (*blue, top*) and in y-plane (*red, bottom*); for proto I (*left*), proto II (*middle*) and the reference detector (*right*) for track at 0° angle.

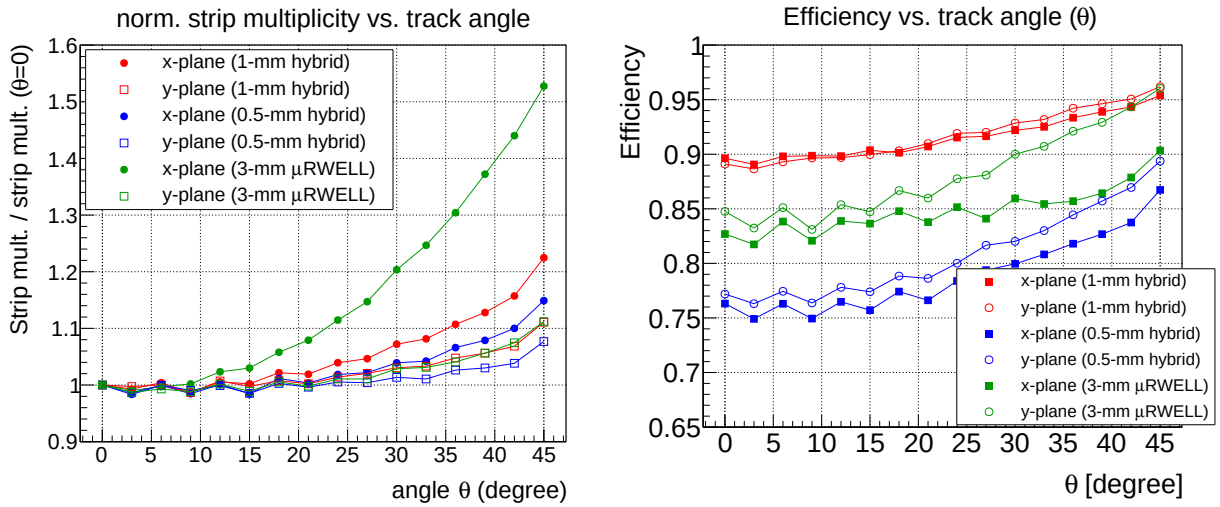

Figure 16: (*right:*) Strip multiplicity as a function of the track angle and normalised to the strip multiplicity at 0° in both x and y planes (*left*); Detector efficiency in x and y planes as a function of the track angle of incoming particle with respect to the detector plane (*right*).

on the plots of Fig. 16. This is an expected result because the path of particle crossing the detector at a

given angle θ is d × $cos(\theta)$ where d is the drift gap of the detector, therefore the probability for ionization is also proportional to d × $cos(\theta)$.

3.4.3 Track fit residuals studies vs. angle scan

The dependence of the spatial resolution of the two thin-gap GEM-μRWELL hybrid prototypes to the incoming track angle of the impinging particles was performed on the setup II of Fig. 9. The two prototypes were installed together with the reference detector on the Y-axis rotation stage. Set of two pairs of upstream GEM trackers and downstream GEM trackers on setup II were installed off of the rotation stage to provide track from the high energy proton beam. Sixteen runs of 25000 triggered events were performed with the X-Y plane of the thin gap prototypes rotating from 0° to 45° in steps of 3°. For the data analysis for each run, events that has a hit recorded simultaneously in all four GEM trackers are selected and the hits are fitted into clean track. The clean track is then projected to the plane of the three detectors under tests . The difference between the projected coordinate from the track fit and the measured coordinate in each X-Y plane of prototypes (also known as track-fit residuals) are stored in a root histogram after a correction is applied to rotate the detector plane back to the its position perpendicular to the beam axis z at 0° angle.

Residuals distribution

The plots in Fig. 17 show the residuals distribution in the x-plane of the detector (the one impacted by the rotation) for proto I (left) and for the reference detector (right) and for tracks at an θ = 0° (top) and θ = 45° (bottom).

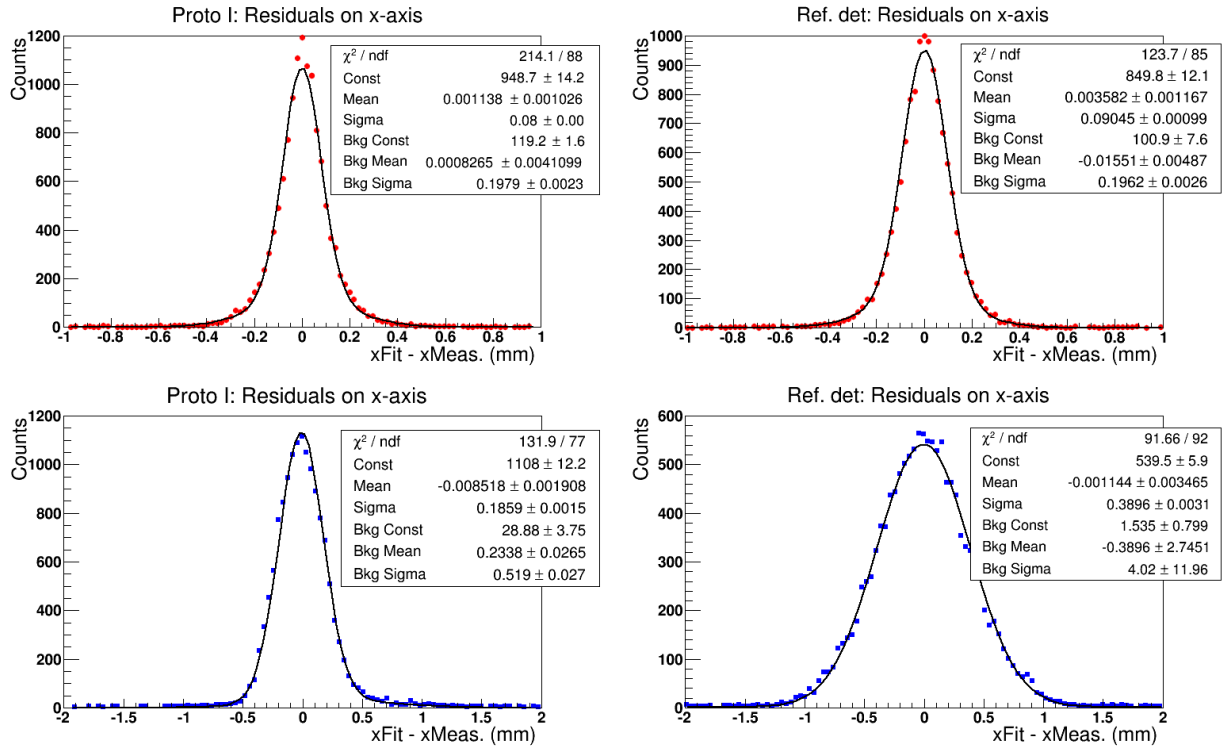

Figure 17: Track fit residuals distribution in x-strip planes of proto I (*left*) and for the reference detector (*right*) for track perpendicular to the detector plane (*red dots, top*) and track angle at 45 degree with respect to the detector plane (*blue dots, bottom*).

The width of the residual distribution is 82μm and 90μm for proto I and reference detector respectively at

$\theta = 0°$ when the detector plane is perpendicular to the particle tracks. For the small angles, the detector spatial resolution is dominated by the geometrical parameter of the strip readout and the charge-sharing of the capacitive-sharing structures. When the particle hit the detectors at a $\theta = 45°$, the width of the residual distribution increases to 186 µm and 390µm for proto I and the reference detector respectively. The width of the residual is significantly larger for the 3-mm drift gap reference detector than for the 1-mm thin-gap prototype which is equal 186µm.

Residual width vs. angle scan

The angle-dependence of the residual widths for the all three prototypes is shown for x-plane and y-planes on right and left plots of Fig. 18 respectively. We observe a quasi-linear dependence of the residual width in x-plane (left plots) with the track angle for all three prototypes while the residuals width is virtually constant for each prototype in the full track angle range. The slope strongly depends on the drift gap of the prototype as expected and is significantly larger for the 3-mm gap reference detector than for the 1-mm gap proto I while the dependence is also more pronounced for the 1-mm gap prototype than for the 0.5-mm gap prototype. This test beam studies clearly demonstrated the benefit of thin-gap MPGDs to limit the impact of large track angle on spatial resolution performance that is one of the limitation of standard gap MPGDs.

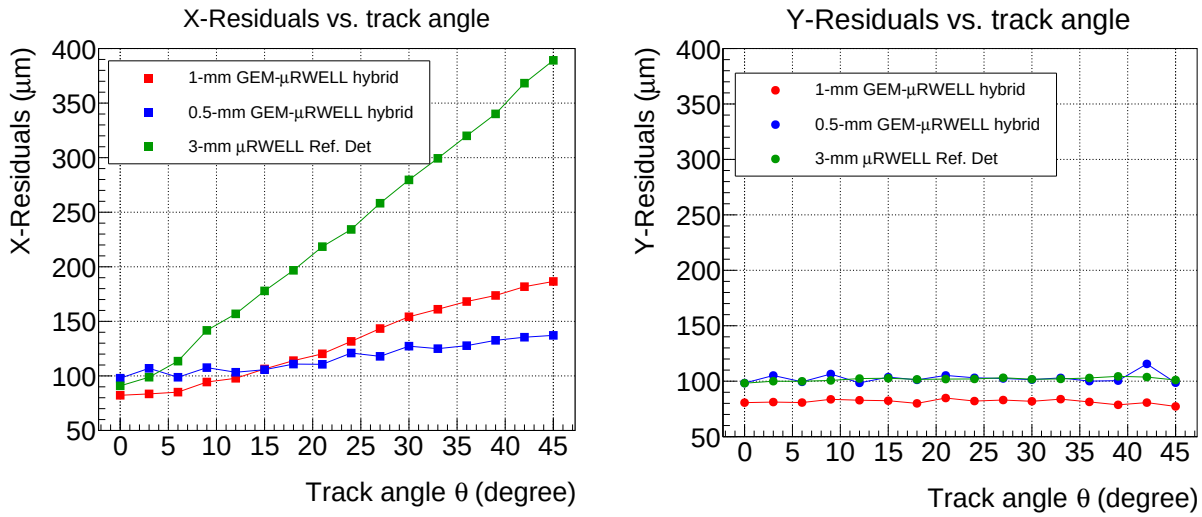

Figure 18: Width of the track fit residuals distribution as a function of the track angle of the incoming particles in x-plane (*left*) and in y-plane (*right*).

3.5 Results with Vanderbilt prototypes

Both the Vanderbilt hybrid thin gap prototypes as listed in table 5 were operated in both Ar-CO_2 80/20 and Kr-CO_2 80/20 gas mixtures for both HV and angle scan. From figure 19 it can be seen that only 64 pins out of 128 pins of the Panasonic connectors are connected to readout strips while the rest of the 64 pins are left floating causing more noise in the chamber. The zero suppression and common mode corrections were determined based on only the strips connected to connectors. More sophisticated method needs to be implemented for zero suppression and common mode correction in future to properly evaluate the performance of the prototypes. In this report the shown performance plots give us only qualitative information about the High Voltage and Angle scan. Fig. 20 shows number of strips fired for normal incidence of beam on both GEM-MMG hybrid and GEM-µRWELL hybrid thin gap prototypes.As can be seen from the figure mostly single strips are being fired making it difficult to differentiate between noise and actual signal.

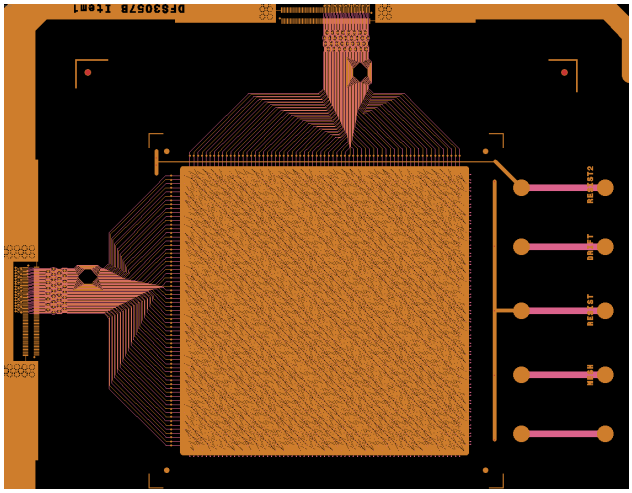

Figure 19: Gerber drawing of the trace of readout board pattern for the Vanderbilt prototypes. As seen in the figure 64 pins of each Panasonic connectors are connected to strips while rest of the pins on each Panasonic connectors were left floating due to design constrain.

3.5.1 Test beam runs

Fig. 21 shows rough estimation of residual distribution for GEM-MMG thin gap prototype in Ar-CO_2 (80:20) gas mixture along both X and Y strips during normal incidence of track on detector plane. The width of residual distribution provides us an estimate of spatial resolution. The residuals shown in fig. 21 was estimated with the requirement of at least 2 strips contributing to cluster formation.

3.5.2 High Voltage Scan studies

The HV scan for the prototypes was done in two stages. In first stage GEM potential across GEM was kept constant while changing the high voltage on μRWELL and MicroMegas. This was done for both Ar-CO_2 and Kr-CO_2 gas mixture. In the second stage voltage across μRWELL and MicroMegas were kept constant while potential difference across GEM foil was varied. This was done only for Kr-CO_2 gas mixture.

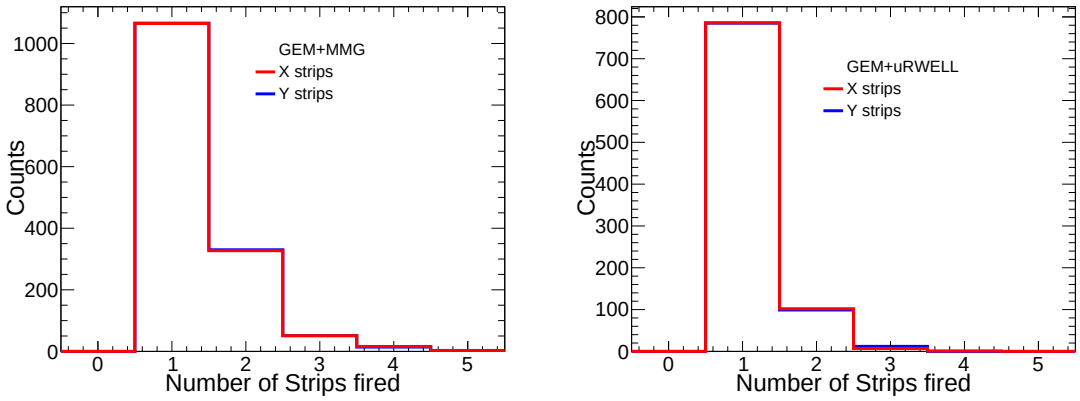

Figure 20: Number of strips contributing to cluster in (*left*) GEM-MMG hybrid thin gap prototype and (*right*)GEM-μRWELL hybrid thin gap prototype in Ar-CO_2 (80:20) gas mixture.

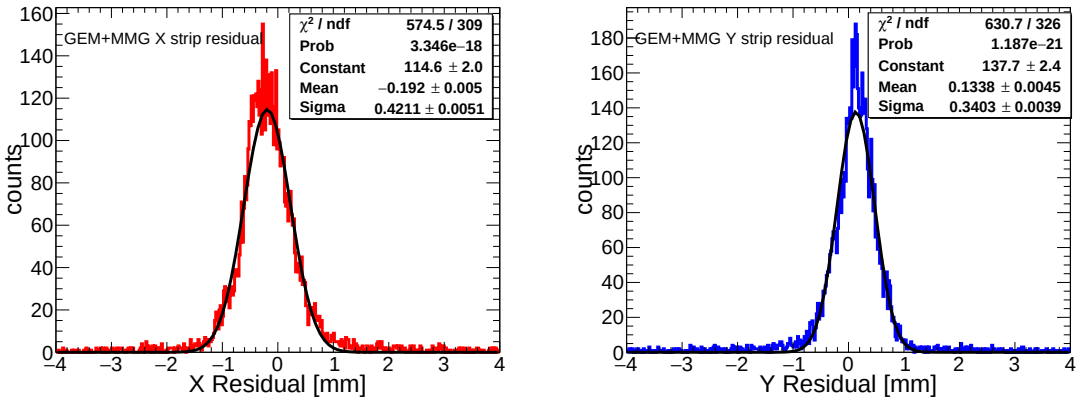

Figure 21: Residual distribution for GEM-MMG hybrid prototype in Ar-CO_2 (80:20) gas mixture at normal incident of test beam in (*left*) X strips and (*right*) Y strips

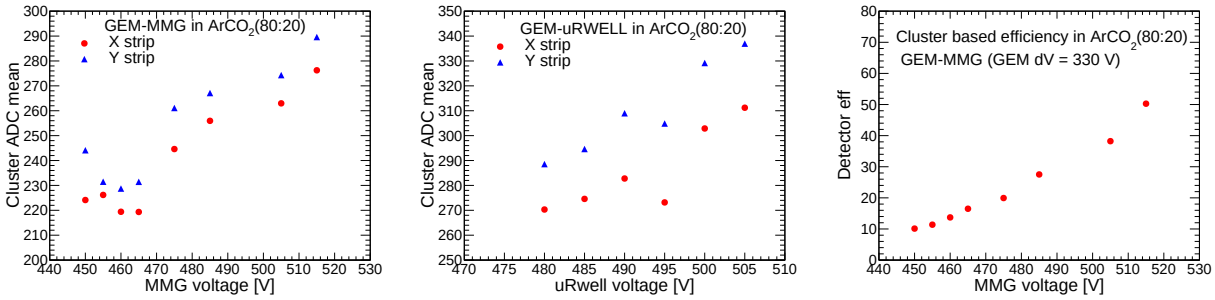

Figure 22: (*left*)Average ADC count in cluster as a function of MMG voltage while keeping potential difference across GEM constant at 330 V in GEM-MMG hybrid prototype operated in Ar-CO_2 (80:20) gas mixture at normal incident of test beam.(*middle*) Average ADC count in cluster as a function of µRWELL voltage while keeping potential across GEM at 330 V. (*right*) Cluster based efficiency of the prototype under same experimental condition.

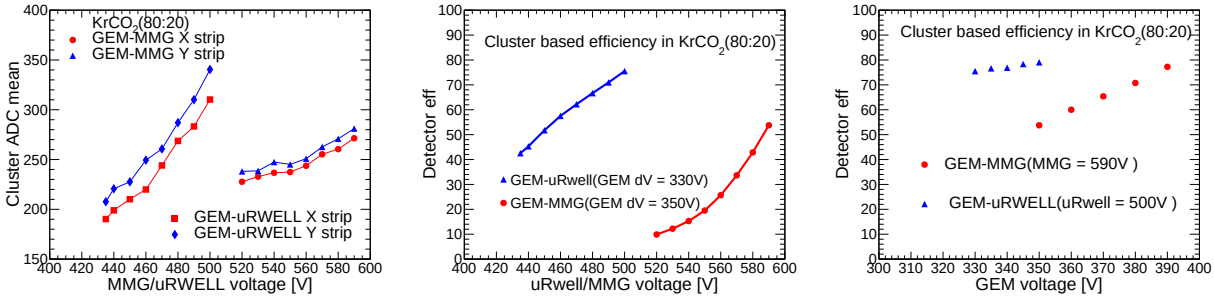

Figure 23: (*left*)Average ADC count in cluster as a function of MMG and µRWELL voltage while keeping potential difference across GEM constant at 330 V in GEM-MMG hybrid prototype operated in Kr-CO_2 (80:20) gas mixture at normal incident of test beam.(*middle*) Cluster based efficiency of the prototype under same experimental condition by varying MMG and µRWELL voltage while keeping GEM voltage constant. (*right*) Cluster based efficiency of the prototype under same experimental condition by varying GEM voltage while keeping MMG and µRWELL voltage constant.

Left hand side of Fig. 22 shows the average ADC count in both X and Y strips as a function of MMG voltage in GEM-MMG prototype in Argon gas mixture. The charge sharing in both X and Y strips do not differ too much. The MMG voltage was varied while keeping the potential across GEM constant at 330 V. The right side of Fig. 22 shows the cluster based efficiency as a function of MMG potential for the same prototype under similar condition. As mentioned earlier special treatment is needed for the prototypes to account for large noise which may explain lower efficiency of the detector.
The results with Kr-CO_2(80:20) gas mixtures are shown in Fig. 23 where the left hand side shows cluster ADC mean value as a function of MMG and μRWELL voltages, middle figure shows cluster based efficiency as a function of MMG and μRWELL voltages while keeping voltage across GEM constant while the right side figure shows cluster based efficiency as a function of GEM layer voltage by maintaining constant voltage for MMG and μRWELL. It can be seeen from cluster ADC mean distribution plots from fig. 22 and fig. 23 that to attain same level of amplification one needs to operate the detector at higher voltage in Kr-CO_2 as compared to Ar-CO_2.

3.5.3 Angle Scan studies

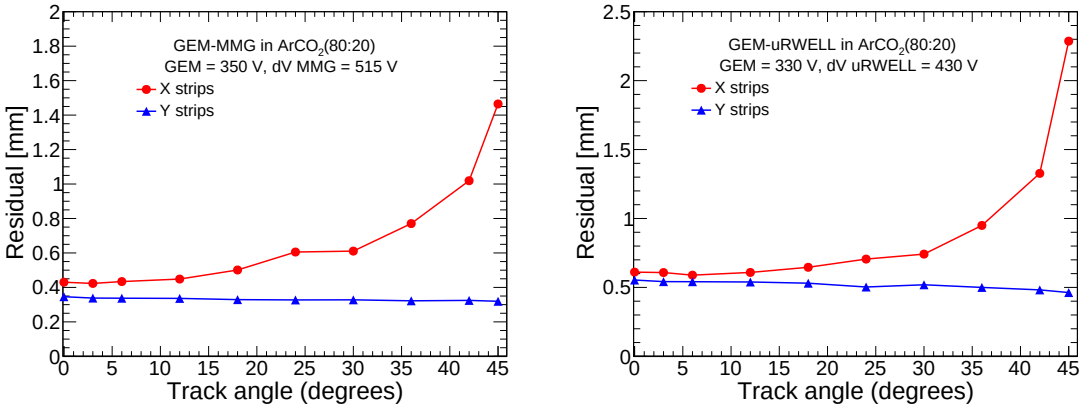

Figure 24: (*left*) Residual dependence on track angle for GEM-MMG prototype in Ar-CO_2 (80:20) gas mixture (*right*) Residual dependence on track angle for GEM-μRWELL hybrid prototype in Ar-CO_2 (80:20) gas mixture .

The performance of the prototypes in terms of spatial resolution as a function of track angle was done by operating the detector at fixed effective gain. The operating voltage was selected based on High Voltage scan results where there is less saturation of electronics which contribute to deterioration of spatial resolution. Fig. 24 shows the dependence of spatial resolution over track angle in Ar-CO_2 (80:20) gas in both X and Y strips. As the detector plane was rotated in X-Y plane with respect to Y axis so as expected there is no effect on spatial resolution of Y strips with track angle. The deterioration of spatial resolution with track angle along X axis for thin gap prototype in fig. 24 is slower as compared to standard 3 mm drift gap detector as shown by green data points in fig. 18. The detector efficiency along with strip multiplicity was also studied for the prototypes and the results are shown in fig. 25. As expected both strip multiplicity and efficiency increases for the prototypes with the increase in track angle over detector surface due to reasons mentioned in section 3.4.3.

3.6 Results with UVa prototypes

To effectively characterize the performance of UVA prototypes, three major contributing factors - the thickness of the drift gap, the gas mixture, and the cathode structure - were considered in the efficiency and spatial resolution studies during the Fermilab test beam. We first performed efficiency measurements on the same

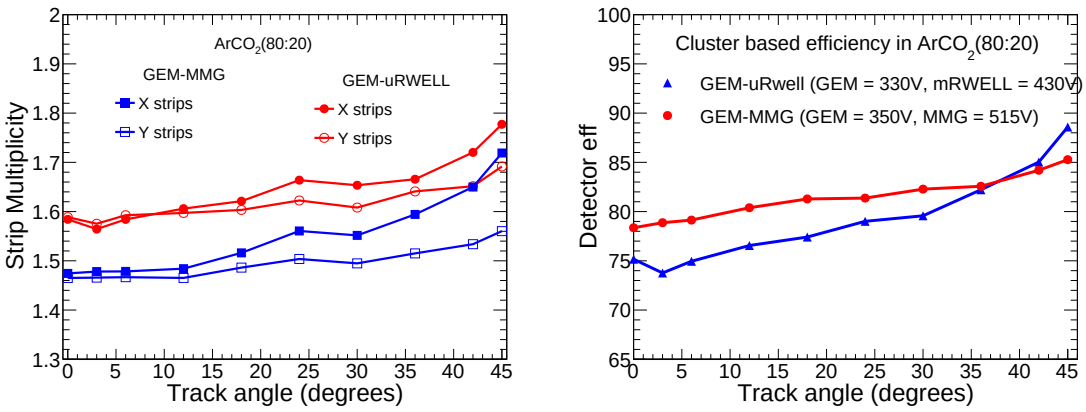

Figure 25: (*left*) Effect of track angle on strip multiplicity on both thin gap GEM-µRWELL hybrid and GEM-MMG prototypes in Ar-CO_2 (80:20)(*right*) Cluster based efficiency as a function of track angle for both GEM-µRWELL hybrid prototype in Ar-CO_2 (80:20) gas mixture .

prototype (Proto II) with two different gas mixtures (Ar-CO_2 & Kr-CO_2), and then on two prototypes with different drift gaps (Proto I & Proto II) but being operated in the same Ar-CO_2 gas mixture, and finally on three prototypes with different cathode structures (Proto I, Proto II & Proto III.) For the spatial resolution studies, we evaluated the dependence of position resolution on the track angle of all four prototypes and the reference detector using the same Ar-CO_2 gas mixture. The spatial resolution of Proto II was investigated with both Kr-CO_2 and Ar-CO_2 gas mixtures. The operational characteristics of the reference detector, a standard triple-GEM detector with a 3 mm drift gap, were used as the baseline to evaluate the impact of reducing the drift gap.

3.6.1 Tracking algorithm in efficiency and spatial resolution studies

Efficiency and resolution studies all rely on the tracking algorithm. In this section, we give a brief introduction to the tracking algorithm we adopted. In this beam test, four chambers were dedicated to tracking, referred to as four trackers, two of them upstream and two of them downstream of the test detectors. A valid track requires at least 1 detected hit on each of the four tracking layers. The tracking in this analysis currently only handles straight-line models. It brute-forces through all possible combinations and compares their χ^2 values. Under high occupancy situations, the brute-force algorithm is time-consuming. To speed up the process, a grid algorithm (initially developed for SBS experiments) is employed, as depicted in Fig.26.

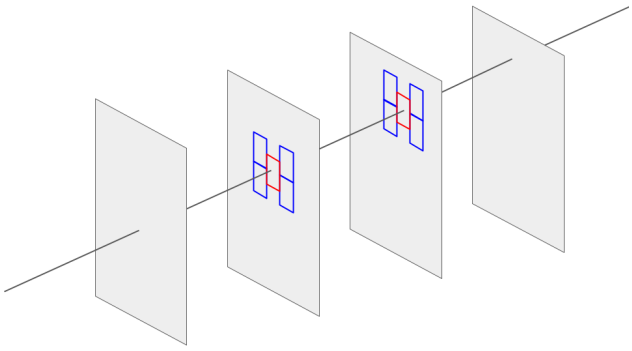

Figure 26: Tracking Algorithm

The tracker planes are segmented into grids, and only hits inside the selected grids will be participating in

the track-finding process. This can greatly reduce the number of possible combinations that the algorithm needs to brute-force. As for this beam test configuration, with no extra constraints to limit the track search region, we only apply the grid to the two inner trackers; all hits on the two outer trackers participate in the track-finding process. The choice of the grid size is a trade-off between the program running speed, the detector offset, and the detector resolution; in this analysis, a grid size of 2 cm by 2 cm is adopted.

The algorithm first loops through all combinations from the two outer tracking layers. For each combination, the program draws a line between the two points and calculates the intersection point on each inner tracking layer. The grid which contains the intersection point will be selected. All hits outside of the selected grid are ignored in the tracking calculation. In cases where the intersection points are very close to the grid edges, a tolerance margin is set up for the grid selection. If the distance between the intersection point and the grid edge is shorter than 1/3 of the grid length, then the neighboring grid will be selected as well, as depicted in Fig.(27). As a result, in one event, the possible number of selected grids is either 1, 2, or 4 grids.

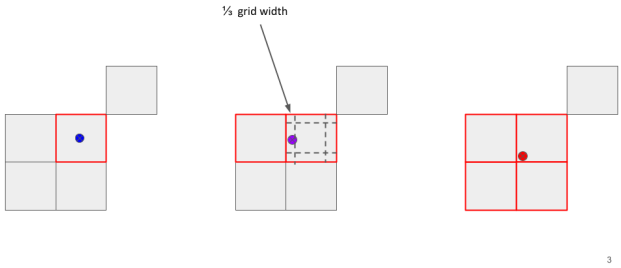

Figure 27: Grid Selection. Red grids are selected. Grey ones are ignored.

To select the cleanest events, we require a good track containing a minimum of 4 hits, which means all 4 trackers have to be fired simultaneously. The tracking algorithm then collects information from these 4 hits and generates the best-fitted track based on the minimum χ^2 requirement. The prototypes under investigation are mounted in between the front trackers and back trackers, and the best-fitted tracks will be used to examine the operational characteristics of the prototypes, including efficiency and position resolution.

3.6.2 Efficiency and stability studies

The efficiency of UVa prototypes was determined based on the track reconstructed from four tracker chambers and the associated hits detected by prototypes under investigation. In the procedure for deriving the track-based efficiency, the best-fit track position projected on each prototype was calculated. Starting from the location of the projected hit, we search for the hits on the prototype within a certain range. If a hit was found within the search area, we consider the prototype detecting the impinging particle; otherwise, we consider it an inefficient event for the prototype. Finally, the prototype's track-based efficiency was defined as the ratio of number of detected hits on the prototype to the number of reconstructed tracks.

For each efficiency study, we scanned the HV applied to the prototype in steps of ≈25V, resulting in steps of ≈ 3V on the HV applied to the middle GEM foil. The maximum and the minimum of HV applied to each prototype were adjusted according to the operating gas mixtures, the drift gap, and the availability of the beam time.

Efficiency vs. Gas mixture study

Our primary study on detector efficiency was dedicated to studying the correlation between the efficiency and the operating gas mixture by comparing detector performance operated in Ar-CO_2 (80%/20%) and Kr-

CO_2 ((80%/20%) gas mixtures. The Ar-CO_2 gas was chosen for its affordability as well as favorable abilities such as non-flammability and non-polymerization. Meanwhile, Kr-CO_2 is a heavier gas and it is chosen to increase the number of primary ionizations to compensate for the drop in the ionization due to the reduced drift gap.

The track-based efficiencies as a function of HV applied to the second GEM foil of Proto II operated in the

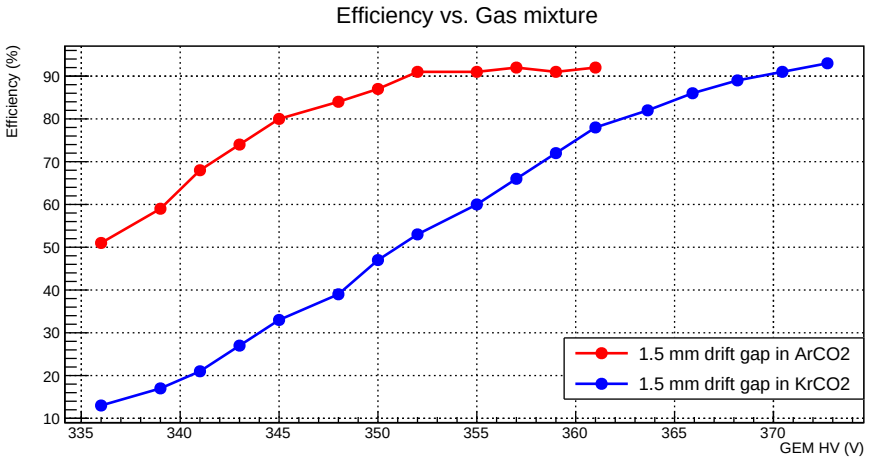

Figure 28: Efficiencies of the triple-GEM prototype with 1.5 mm drift gap in Ar-CO_2 and Kr-CO_2 gas mixtures

two different gas mixtures are shown in Fig. 28. The blue is for Kr-CO_2 gas and the red is for Ar-CO_2 gas. Our results show that the 1.5 mm drift gap detector was able to reach a reasonably high efficiency of 92% in the more affordable Ar-CO_2 gas and at a HV applied to the second GEM foil much lower than what is needed for the Kr-CO_2 gas (352V vs. 382V.) On the other hand, the same detector operated in Kr-CO_2 gas already had an efficiency as high as 94% even before reaching the plateau.

The detector operated in Kr-CO_2 could have been brought to full efficiency by either increasing the HV applied to the GEM foils or further optimizing the ratio in the gas mixture. However, due to limitations on gas resources, the beam time, and the mechanism that we used to power our prototypes at the Fermilab beam test, we did not push for the plateau during our Fermilab beam test. Further studies on optimizing on ratio of gas mixture and strength of electric field applied to GEM foils and drift region for detector stability, especially in the high-rate environment, can be done in our lab at UVA using the X-ray and Sr sources.

Efficiency vs. Drift Gap study

To evaluate the impact of reducing the drift gap on MPGDs detection ability, plateaued efficiencies of prototypes with different drift gaps were measured in the test beam and compared to the efficiency of the standard 3mm drift gap triple-GEM detector. Fig. 29 shows efficiencies as a function of HV applied to the second (middle) GEM foil of Proto I and Proto II operated in Ar-CO_2 (80%/20%) gas mixture. The voltages for the other GEM foils and gaps were also varied in proportion to the second GEM foil HV shown in the plots. The red and the blue are for Proto I and Proto II with 1.0 mm and 1.5 drift gaps, respectively. Our studies show that triple-GEM detectors operated in Ar-CO_2 gas and having a drift gap as thin as 1.0 mm (1.5 mm) were capable of achieving an efficiency of 90% (92%). Further optimizing the gas mixture ratio could help to bring the efficiency of thin-gap triple-GEM detectors closer to the efficiency of 96% of a standard 3mm drift gap triple-GEM detector.

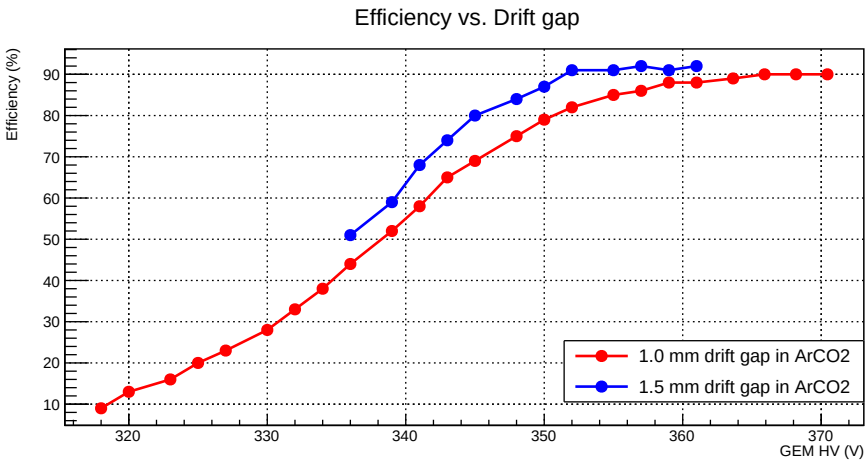

Figure 29: Efficiencies of prototypes with 1.0 mm & 1.5 mm drift gaps in Ar-CO_2 gas

HV Stability of prototypes with wired cathodes

Considering the difficulties that may arise in operating large-area thin-gap MPGDs, especially in a high-rate environment, we explored the use of cathodes made of fine wire to ensure a constant drift gap throughout a large area. The performance in terms of stability, detection efficiency, and spatial resolution of prototypes having wire cathodes was investigated during our test beam.
However, an unexpected problem with the Fermilab gas system during the data-taking process for Proto III and Proto IV (with the wire cathode) led to unstable gas flow through the 4 trackers, and we were unable to derive the efficiency of these prototypes. Our investigation on the HV stability of these prototypes was carried out solely based on the cluster information of each prototype. We first reconstructed the clusters on the 2D-trips strips of the RO board and then applied a series of cuts on cluster size, timing, and strip ADC correlation to filter the clusters. If the clusters on x- and y-strips survived these selective cuts, we consider the prototype to have fired for the event. The cluster multiplicity-based efficiency, which is defined as the ratio of fired events to the total triggers in each run is used to evaluate the performance of these prototypes.

Fig. 30 shows the propagation of the cluster-based efficiencies as a function of the HV applied to the middle GEM foil. In the setup for this study at the test beam, the gas line was connected to Proto III and Proto IV in series where the output gas line of Proto III was also the input gas line of Proto IV. Due to the gas leak of Proto III, the cluster-based efficiency of Proto IV was lower than that of Proto III and reached the plateau at a higher GEM HV. Our result indicates that even with the drift gap as thin as 1.5 mm, the prototypes with wired cathode were comfortably operated with the electric field applied to GEM foils and drift volume 25% higher than the standard operating electric field strength in the triple-GEM detectors with a standard 3 mm drift gap.

3.6.3 Spacial resolution studies

The setup II described in section 3.1 was used for our studies on the track angle dependence of the spatial resolution of thin-gap triple-GEM prototypes and to examine the influence of operating gas and cathode structure on the spatial resolution. The setup was arranged such that the beam was parallel to the z-direction, all four trackers were in the x-y plane, and the prototypes under examination could be rotated around the y-axis at an angle θ ranging from 0^o to 45^o as indicated in Fig. 31. In the test beam, the rotating angle θ in setup II presented the track angle impinging prototypes mounted on the rotation stand, and as the x-, y-, z-axis defined on the sketch in Fig. 31, the x-spatial resolution of prototypes would be affected the most as the angle θ increases.

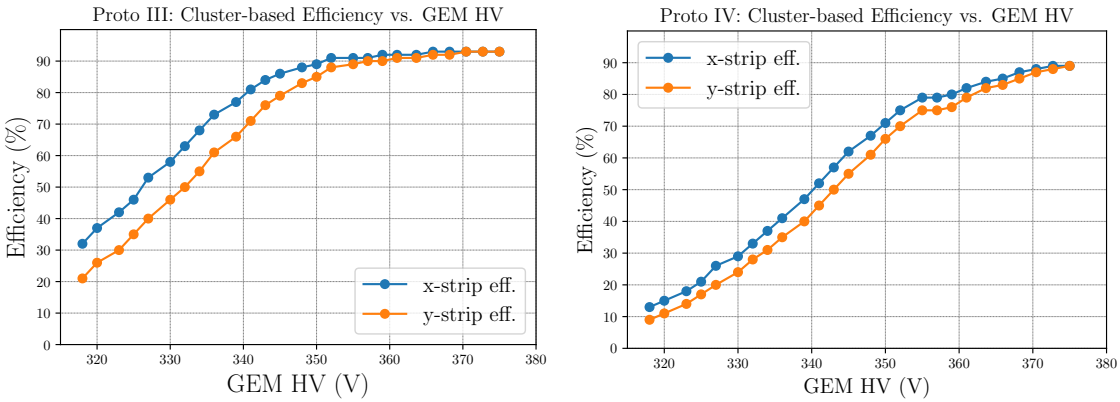

Figure 30: Cluster-based efficiency as a function of HV applied to the middle GEM foil of a prototype with 400 μm wire-pitch cathode (*left*), and 800 μm wire-pitch cathode (*right*).

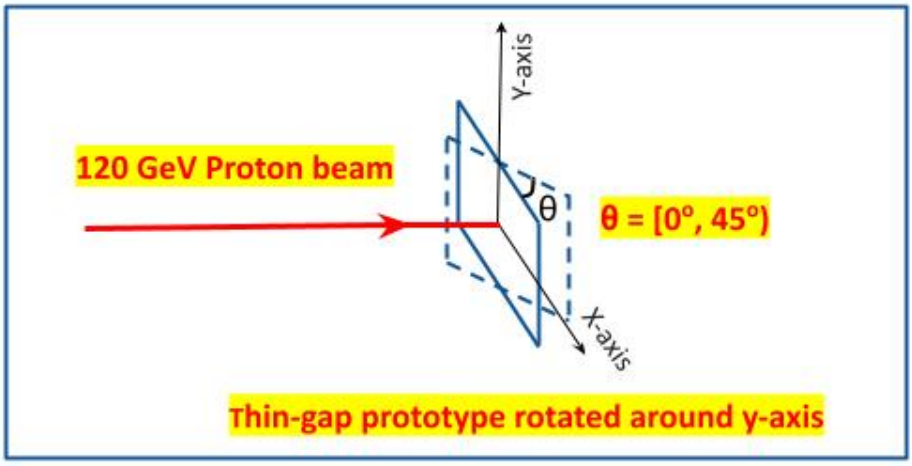

Figure 31: Rotation of prototypes in spatial resolution studies

Similar to the analysis procedure for efficiency studies, the bested-fit track constructed from the hits on four trackers was projected to the plane of the prototype under examination to find the predicted track position, and then the residual of the detected hit associated with this track was calculated as the difference between the detected hit and the predicted track position on the prototype. The width of the residual distribution generated for each run at the test beam can be used to evaluate the spatial resolution of the prototype.

Spatial resolution vs. track angle & drift gap

Our primary focus of spatial resolution studies was on investigating the correlation between the thickness of the drift gap and spatial resolution, especially at large track angles. In this study, we characterized the position resolution performance of three prototypes having the same cathode structure but different drift gaps as the track angle spanned from 0^o to 45^o.

The set of plots in Fig. 32 show the distributions of hit-residuals in the x-direction for Proto I (left), Proto II (center), and the reference detector (right) at angles $\theta = 0^o$(top plots) and $\theta = 45^o$ (bottom plots). All three prototypes involved in this study were operated in Ar-CO_2 gas and have cathodes made of Kapton-Copper

foil, but their drift gap varies in the range from 1 mm - 3 mm. At $\theta = 0^o$, regardless of the drift gap, the widths of the x-residual distributions of three prototypes were very similar (67µm, 65µm, and 68µm for prototypes with 1.0 mm, 1.5 mm, and 3.0 mm drift gap, respectively.) The reason behind this similarity is that at a small track angle, the position resolution of a triple-GEM detector is mainly determined by the structure of the readout board. With the track angles increased to $\theta = 45^o$, the width of the x-residual distributions increased for all three prototypes as expected, with the larger increase in the width of the x-residual for the larger drift gaps (182µm, 267µm, and 505µm for prototypes with 1.0 mm, 1.5 mm, and 3.0 mm drift gap, respectively.) This result indicates that as the drift gap reduced from 3.0 mm to 1.0 mm, the spatial resolution was improved by a factor close to 3.

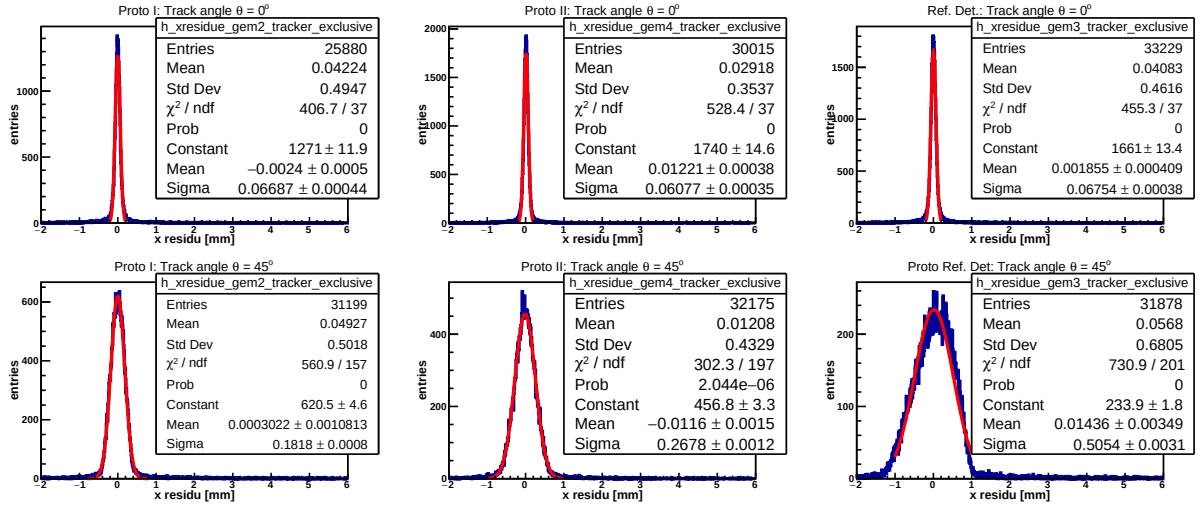

Figure 32: X-residual distribution for Proto I with 1 mm drift gap (*left*), Proto II with 1.5 mm drift gap (*middle*), the Ref. Det with 3 mm drift (*right*) at track angles $\theta = 0^o$(top) and $\theta = 45^o$ (bottom)

The two plots in Fig. 33 show the track angle dependence of the sigma of distribution of hit-residuals in the x- and y-directions for three detectors with different drift gaps while being operated with the same Ar-CO_2 gas mixture. The red, green, and blue dots in these plots represent data of Proto I, Proto II, and reference detector with drift gap of 1.0 mm, 1.5 mm, and 3.0 mm, respectively. The plot on the left of Fig. 33 shows that the x-spatial resolution of all three prototypes deteriorates as the track angle increases. Furthermore, the larger the drift gap, more rapidly the spatial resolution gets worse. We expect this because increasing either the angle θ or the drift gap elongates the trail that particles traverse in the drift volume before reaching the amplification stage. This causes more primary ionization to happen along the trail and a larger number of RO strips to be fired for an associated event, and subsequently, decreasing the spatial resolution.

As shown in the plot on the right of Fig. 33, the y-spatial resolutions of all three prototypes are nearly unchanged over a broad range of track angle θ, and there is only a minor deterioration towards larger angles. This is an expected result given that the beam was along the z-axis and the prototypes were rotated around the y-axis, as depicted in the sketch in Fig. 31. Thus, the y-spatial resolution is mainly determined by the structure of RO board. The minor deterioration towards larger angles could mostly be due to the imperfect alignment wherein the angle between the y-axis and the prototype plane slightly deviates from 0.

From the result of this study, we conclude that reducing the drift gap of MPGDs is crucial to improving space resolution at large track angles.

Spatial Resolution vs. track angle & gas mixture

To evaluate the impact of the operating gas mixture on the spatial resolution of the thin-gap MPGDs, we performed the analysis on the distribution of hit-residuals from the predicted track position of Proto II (1.5

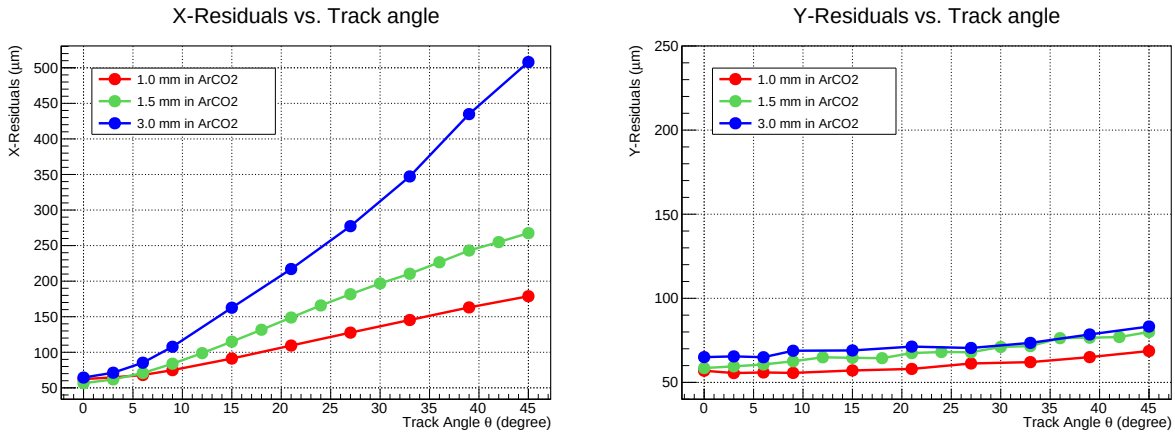

Figure 33: Sigma of distribution of the x-residuals (*left*) and y-residuals (*right*) from the predicted track position as a function of track angle for Proto I (1mm drift gap), Proto II (1.5mm drift gap) and Ref. Det((3mm drift gap)

mm drift gap) with two different gas mixtures at the track angles ranging from 0^o to 45^o. The two plots in Fig. 34 show the track angle dependence of the sigma of distribution of hit-residuals in the x- and y-direction from the predicted track position for Proto II operating with Ar-CO_2 gas (red) and Kr-CO_2 gas (blue). Our result reveals that, in terms of spatial resolution, the performance of the thin-gap Triple-GEM detector is nearly independent of whether it is operated in Ar-CO_2 (80%, 20%) or Kr-CO_2 (80%, 20%).

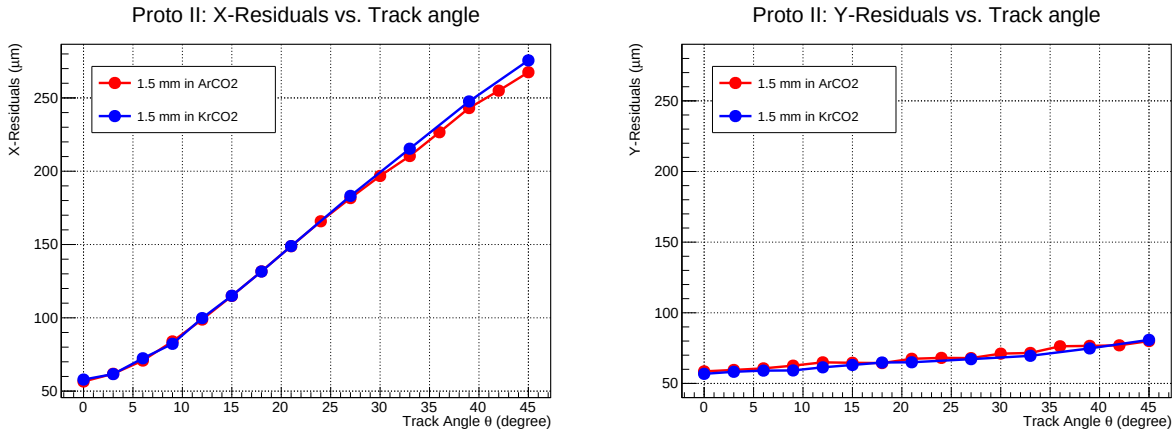

Figure 34: Sigma of distribution of the x-residuals (*left*) and y-residuals (*right*) from the predicted track position as a function of track angle for Proto II (1mm drift gap) in Ar-CO_2 and Kr-CO_2 gas mixtures

Spatial Resolution vs. track angle & cathode structure

The two plots in Fig. 35 show the track angle dependence of the sigma of distribution of hit-residuals in the x- and y-directions from the predicted track position for prototypes with three different cathode types: Kapton foil with 5 μm Cu coating (Proto III), 400 μm pitch wire layer (Proto III), and 800 μm wire layer (Proto IV). All three prototypes had a drift gap of 1.5 mm and were operated with Ar-CO_2 gas. In general, the behavior of the x-spatial resolution and y-spatial resolution for the three prototypes are almost the same, such that the x-spatial resolutions significantly worsen as the track angle increases and the y-spatial resolution while the y-spatial resolutions of each prototype are just slightly changed over a broad range of track angle θ.

In the case of the x-spatial resolutions for small angles up to approximately $\theta < 10^o$ and y-spatial resolution over the entire angle range from 0^o to 45^o, the resolutions for the wire cathodes are worse than for the Kapton-Cu foil cathode, while the 800 μm wire cathode has worse resolution than the 400 μm wire cathode. This result is to be expected given that the foil cathode provides a uniform drift electric field while the discrete structure of the wire cathodes leads to non-uniformities of the drift field, with this effect increasing with the wire pitch.

Our results also show that for track angle $\theta > 10^o$, the x-spatial resolution for the 400 μm wire cathode becomes comparable to that for the foil cathode. This could be due to the fact that for large track angles, the track passes through the electric field created by more than one cathode wire, thereby leading the field's non-uniformity effects to be averaged out. However, this does not explain the improvement in the x-spatial resolution for the 800 μm cathode for track angle $\theta > 10^o$. This improvement could be due to effects associated with the setup such as the orientation between the parallel wires on the cathode layer and the x-strips on the RO board or some uncertainties on positioning the prototype and need to be further investigated.

Overall, the high efficiency, the good spatial resolution, and the good HV stability the wire cathodes yield demonstrate that wire cathodes with pitch up to 800 μm are a viable alternative to foil-based cathodes for thin-gap MPGDs.

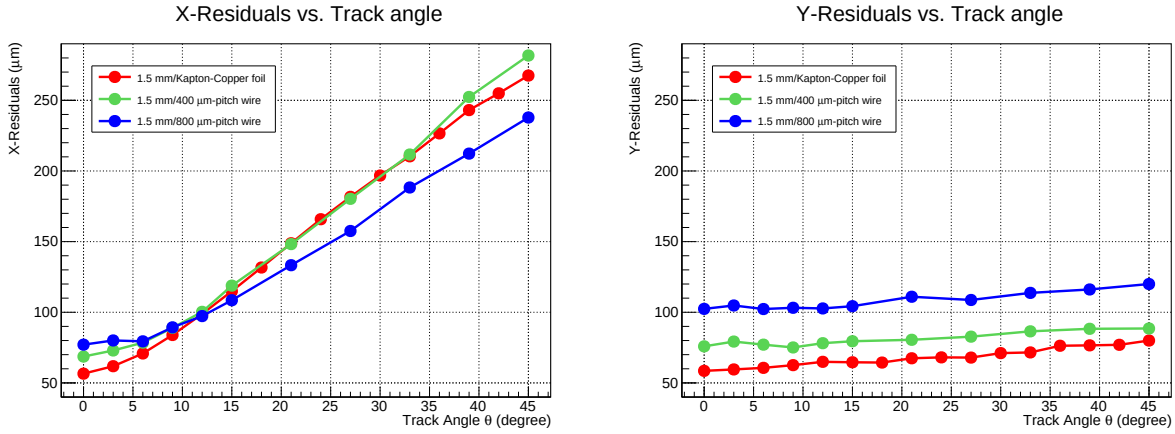

Figure 35: Sigma of distribution of the x-residuals (*left*) and y-residuals (*right*) from the predicted track position as a function of track angle for Proto II, Proto III and Proto IV with the same drift gap

3.7 Results with Yale Cosmic setup

The Yale team (in cooperation with BNL) had an idea to test a small (10 cm × 10 cm) Micromegas (MMG) chamber with a 1 mm ionization gap. But at the last moment it was found that we have (available) only a chamber prepared for TPC readout (specifics size and shape readout pad structure). That is why a decision was made not to use this chamber during a test beam, but prepare a cosmic setup to measure / estimate a tracking efficiency to (mainly) muons. The chamber was assembled with an additional GEM foil, with 1.2 mm (frame thickness) gap from MMG mesh, plus the cathode electrode with 3.4 mm gap in the same gas vessel. Four Scintillator counters (9 cm × 9 cm, two on top and two at the bottom of the MMG prototype under study, were used as a Cosmic trigger when all four signals were in a coincidence ("S"). The MMG mesh was connected to the Charge sensitive PA and followed by a fast amplifier / shaper / discriminator. It allows organizing a logical response (Y/N) for the signal amplitude more than controlled threshold ("M") and "slow" spectrometric output to MCA with / without outside trigger ("A"). Fe55 source, calibrated capacitor and step voltage pulser were used to measure a gas gain. All measurements were made with the same "effective" gas gain close to 3.e4. Tracking efficiency measurements were done in a "reference" mode. As a first step the gas gain was on only rising a MMG mesh voltage and using a GEM as a Cathode. Number of events

(SxM) and S were recorded with the label – "1.2 mm". Then the MMG voltage was down, but GEM and Cathode (3 Voltages) were tuned to restore a gas gain. Once more another record was done for the ratio (SxM)/S with the label – "3. mm". The ratio for these two measurements was used as a tracking efficiency for the 1.2 mm ionization gap. The tracking efficiency estimation for Cosmic Muons: ((SxM)/M) "1.2 mm" / ((SxM/M) "3. mm": 0.87+/-0.03 (0.8 Ar + 0.2 CO2). 0.91+/-0.04 (0.9 Ar + 0.1 isoButane).

To simulate the proposed "Double Thin-Gap " MPGD the second MMG chamber was prepared with 1. mm ionization gap, and it was installed on the "top" of the second one. Logical signals from first and second chambers were combined as "OR", and the same two steps measurements were done. The "Double Thin-Gap" tracking efficiency estimation for Cosmic Muons: 0.96+/-0.03 (0.8 Ar + 0.2 CO2); 0.975+/-0.03 (0.9 Ar + 0.1 isoButane).

4 Summary & what is planned next

Our R&D goal for the FY22 proposal was to demonstrate the validity of the concept of thin-gap MPGDs (tg-MPGDs) and demonstrate that excellent spatial resolution is still possible for MPGDs in this configuration for track impinging the detectors at large angle. Several small (active area of 10 cm $\times$ 10 cm) thin-gap MPGD prototypes were built in the various institutions in the thin-gap MPGD consortium and tested in the 120 GeV proton beam at the Fermilab Test Beam Facility (FTBF) in June 2023. Preliminary data analysis of test beam results successfully demonstrate that thin-gap MPGD technologies based on standard triple-GEM amplification or the novel approach of GEM-μRWELL (or GEM-Micromegas) hybrid technologies for double amplification can achieve a spatial resolution better than 200 μm for track at 45^o degree angle and better than 130 μm on average in the full η-range in the barrel region of a collider detector. Detector efficiency of up to 90% was reached with the thin-gap prototypes when operating with standard low cost Ar-CO_2 80/20 gas mixture. Efficiency higher than 96% is expected for heavier gas based mixture such as Xe-CO_2 or Kr-CO_2 albeit at higher voltage operating point and significantly higher cost.
The excellent results obtained with the proof-of-concept small prototypes open the possibility to explore the development of large area thin-gap MPGD for applications as tracking layers in future NP and HEP experiments. Large and even thinner drift gap (0.5 mm) prototypes operating in the double-sided configuration are under development as continuation of this current EIC Generic R&D program. The link of the FY23 medium-size thin-gap hybrid MPGDs proposal is found below FY23 Thin-gap MPGD proposal. Thin-gap hybrid MPGDs will undoubtedly plays a major role in gas-based tracking detectors for EIC ePIC detector and EIC second detector, but the thin-gap MPGD technology will also provide options for high performance tracking for future NP experiments at Jefferson Lab such as additional tracking layers to SoLID triple-GEM trackers.

References

[1] R. Abdul Khalek et al. *Science Requirements and Detector Concepts for the Electron-Ion Collider: EIC Yellow Report*. 2021. DOI: 10.48550/ARXIV.2103.05419. URL: https://arxiv.org/abs/2103.05419.

[2] Kondo Gnanvo et al. "Performance of a resistive micro-well detector with capacitive-sharing strip anode readout". In: *Nuclear Instruments and Methods in Physics Research Section A: Accelerators, Spectrometers, Detectors and Associated Equipment* (2022), p. 167782. ISSN: 0168-9002. DOI: https://doi.org/10.1016/j.nima.2022.167782.

[3] C. Altunbas et al. ""Construction, test and commissioning of the triple-gem tracking detector for compass"". In: *Nucl. Instrum. Meth.* A490.1 (2002), pp. 177–203. ISSN: 0168-9002. DOI: https://doi.org/10.1016/S0168-9002(02)00910-5. URL: http://www.sciencedirect.com/science/article/pii/S0168900202009105.

[4] M.J. French et al. "Design and results from the APV25, a deep sub-micron CMOS front-end chip for the CMS tracker". In: *Nuclear Instruments and Methods in Physics Research Section A: Accelerators, Spectrometers, Detectors and Associated Equipment* 466.2 (2001). 4th Int. Symp. on Development and Application of Semiconductor Tracking Detectors, pp. 359–365. ISSN: 0168-9002. DOI: https://doi.org/10.1016/S0168-9002(01)00589-7.

[5] J. Toledo S. Martoiu H. Muller. "Front-end electronics for the Scalable Readout System of RD51". In: *2011 IEEE Nuclear Science Symposium Conference Record*. 2011, pp. 2036–2038. DOI: 10.1109/NSSMIC.2011.6154414.

[6] *RD51 collaboration: Development of Micro-Pattern Gas Detectors Technologies*. https://rd51-public.web.cern.ch/. 2008.

[7] ALICE DAQ Projects. "ALICE DAQ and ECS Manual". In: *ALICE Internal Note* DAQ ALICE-INT-2010-001 (2010).

[8] W. Xiong et al. "A small proton charge radius from an electron–proton scattering experiment". In: *nature* 575 (2019), pp. 147–150. DOI: https://doi.org/10.1038/s41586-019-1721-2.

[9] *Upgrade of SRS Electronics for PRad GEMs readout*. https://indico.cern.ch/event/496113/contributions/2008305/attachments/1240667/1824222/KG_RD51CollMeeting20160309_WG5.pdf. 2016.